

Hydrodynamic equations for self-propelled particles: microscopic derivation and stability analysis

This content has been downloaded from IOPscience. Please scroll down to see the full text.

2009 J. Phys. A: Math. Theor. 42 445001

(<http://iopscience.iop.org/1751-8121/42/44/445001>)

View [the table of contents for this issue](#), or go to the [journal homepage](#) for more

Download details:

IP Address: 169.230.243.252

This content was downloaded on 27/12/2014 at 19:52

Please note that [terms and conditions apply](#).

Hydrodynamic equations for self-propelled particles: microscopic derivation and stability analysis

Eric Bertin^{1,2}, Michel Droz² and Guillaume Grégoire³

¹ Université de Lyon, Laboratoire de Physique, ENS Lyon, CNRS, 46 Allée d'Italie, F-69007 Lyon, France

² Department of Theoretical Physics, University of Geneva, CH-1211 Geneva 4, Switzerland

³ Laboratoire Matière et Systèmes Complexes (MSC), UMR 7057, CNRS-Université Paris-Diderot, F-75205 Paris Cedex 13, France

E-mail: eric.bertin@ens-lyon.fr

Received 27 July 2009

Published 8 October 2009

Online at stacks.iop.org/JPhysA/42/445001

Abstract

Considering a gas of self-propelled particles with binary interactions, we derive the hydrodynamic equations governing the density and velocity fields from the microscopic dynamics, in the framework of the associated Boltzmann equation. Explicit expressions for the transport coefficients are given, as a function of the microscopic parameters of the model. We show that the homogeneous state with zero hydrodynamic velocity is unstable above a critical density (which depends on the microscopic parameters), signalling the onset of a collective motion. Comparison with numerical simulations on a standard model of self-propelled particles shows that the phase diagram we obtain is robust, in the sense that it depends only slightly on the precise definition of the model. While the homogeneous flow is found to be stable far from the transition line, it becomes unstable with respect to finite-wavelength perturbations close to the transition, implying a non-trivial spatio-temporal structure for the resulting flow. We find solitary wave solutions of the hydrodynamic equations, quite similar to the stripes reported in direct numerical simulations of self-propelled particles.

PACS numbers: 05.70.Ln, 05.20.Dd, 64.60.Cn

(Some figures in this article are in colour only in the electronic version)

1. Introduction

In the recent years, a lot of effort has been expended with the aim of explaining the collective behaviour of living systems [1]. Such collective behaviours can be observed on many different scales including mammal herds [2], crowds of pedestrians [3, 4], bird flocks [5], fish schools

[6], insect swarms [7], colonies of bacteria [8], molecular motors [9, 10] and even interacting robots [11]. It turns out that the collective properties of such systems seem to be quite robust and universal. Accordingly, this field attracted the interest of the statistical physics community with the challenge of introducing minimal models that could capture the emergence of collective behaviour. One important class of models consists of the so-called self-propelled particle models, for which the onset of collective motion without a leader is present. Vicsek *et al* [12, 13] introduced a simple model defined on a continuous plane, where agents (or animals) are represented as point particles with a velocity of constant amplitude. Noisy interaction rules tend to align the velocity of any given particle with its neighbours. Extensive numerical simulations of this model have been performed [14, 15], showing the presence of a phase transition from a disordered state, at high enough noise, to a state with collective motion. A different approach is to consider the problem at a coarse-grained level and to describe the dynamics in terms of hydrodynamic fields. The equations governing the evolution of these hydrodynamic fields can be either postulated phenomenologically [16], on the basis of symmetry and conservation laws considerations [17, 18], or derived from specific microscopic models [19, 20]. The equations of motion of the hydrodynamic field are derived from the microscopic model through a Boltzmann approach.

Following an earlier publication [19], the motivation of the present work is to derive, from a microscopic model, the hydrodynamic equations describing at a coarse-grained level the flow of self-propelled particles (SPP) and to compare the resulting description with numerical simulations of an agent-based model of SPP. The analytical framework we use is that of the Boltzmann equation. Accordingly, a suitable microscopic model for such a treatment is a continuous time model with interactions reducing to binary collisions. In order to show that the most salient features of the coarse-grained analytical description are not specific to a binary collision model, we use for the numerical simulations a standard agent-based model [12, 13] that has been well characterized in the literature [14, 15]. Note that some comparison with numerical simulations of an agent-based model with binary interaction have already been presented in [19].

2. Microscopic models of interacting self-propelled particles

2.1. Definition of the models

2.1.1. Continuous time model with binary collisions. Following [19], we introduce a simple model that captures the essential physics of assemblies of self-propelled particles, while being suitable for a description in terms of a Boltzmann equation. We consider the evolution of self-propelled point-like particles on a two-dimensional plane. The displacement of each particle i is governed by a velocity vector \mathbf{v}_i . In order to account for the self-propelling property, we assume that the modulus of the velocity vector is fixed to a value v_0 , identical for all the particles, so that only the direction of the vector plays a role in the dynamics. The relevant dynamical variables are then the angles θ_i that the vectors \mathbf{v}_i form with a fixed reference direction. It is important to note, at this stage, that fixing the modulus of the velocity breaks the Galilean invariance of the system. Hence one should not expect that the eventually obtained hydrodynamic equations obey such an invariance, contrary to what happens in usual flows.

Apart from the ballistic evolution according to their velocity vector, particles also experience stochastic events that punctuate their dynamics. These stochastic events are of two different types. The simplest ones are self-diffusion events, that is, the angle θ of an isolated particle changes, with a probability λ per unit time, to $\theta' = \theta + \eta$, where η is a

noise with distribution $p_0(\eta)$ and variance σ_0^2 . In the following, we consider a Gaussian distribution for $p_0(\eta)$, also taking into account the periodicity of θ . This type of stochastic events lead to a diffusive behaviour at large scale, thus preventing the system from having a trivial (pseudo)collective motion, of purely ballistic nature. To drive the system into an organized state where a genuine collective motion sets in, one has to introduce interactions between the particles. Given that we wish to use a Boltzmann approach to study the model, it is natural to consider binary interactions between particles. These binary interactions are introduced as follows. When two particles get closer than a threshold distance d_0 , their velocity angle θ_1 and θ_2 are changed into θ'_1 and θ'_2 according to

$$\theta'_1 = \bar{\theta} + \eta_1[2\pi], \quad \theta'_2 = \bar{\theta} + \eta_2[2\pi], \quad (1)$$

where $\bar{\theta}$ is defined by

$$\bar{\theta} = \arg(e^{i\theta_1} + e^{i\theta_2}). \quad (2)$$

The noises η_1 and η_2 are independent Gaussian variables with variances σ^2 . Note that σ^2 may differ from the variance σ_0^2 of the noise associated with the self-diffusion of particles.

2.1.2. Agent-based model for numerical simulations. In order to compare the results of the analytical approach based on the binary collision model to direct numerical simulations, we use a slight generalization of the standard Vicsek model [12, 13]. The motivation for simulating numerically a model different from the one we used in the analytical approach is twofold. First, the Vicsek model has been thoroughly characterized in the literature [13–15], making it a useful benchmark for comparison. Second, and most importantly, a model with continuous time dynamics and binary collisions is well-suited for a Boltzmann equation approach, but very inefficient from the point of view of direct numerical simulations. In contrast, the Vicsek model, with a discrete time dynamics and multi-neighbour interactions, is much more efficient to simulate.

The agent-based model that we consider consists of N particles on a two-dimensional space of area $L \times L$, with periodic boundary conditions. Each particle j at any instant t has a constant modulus speed v_0 . This property allows the mapping of velocity on complex numbers. Then a particle is located by a two-coordinate vector \mathbf{x}_j^t and an angle θ_j^t which gives its speed direction. We define the vicinity \mathcal{V}_j^t of j at time t as the disc centred on j with a radius d_0 . Then the direction of j at the next instant $t + \Delta t$ is simply the direction of the averaged speed over all particles which are embedded in its vicinity, including j itself, up to a noise term. If there is no neighbour in the disc of interaction, self-diffusion occurs randomly:

$$\theta_j^{t+\Delta t} = \begin{cases} \arg \left[\sum_{k \in \mathcal{V}_j^t} e^{i\theta_k^t} \right] + \eta \xi_j^t, & \text{if } \mathcal{V}_j^t \neq \{j\}, \\ \theta_j^t + \eta_0 \xi_j^t, \text{ with probability } \lambda \Delta t, & \text{if } \mathcal{V}_j^t = \{j\}, \\ \theta_j^t, \text{ with probability } 1 - \lambda \Delta t, & \text{if } \mathcal{V}_j^t = \{j\}, \end{cases} \quad (3)$$

$$\mathbf{x}_i^{t+\Delta t} = \mathbf{x}_i^t + v_0 \mathbf{e}(\theta_i^{t+\Delta t}) \Delta t, \quad (4)$$

where $\mathbf{e}(\theta)$ is the unit vector of direction θ . The parameters η and η_0 are the noise amplitudes for collision and self-diffusion, respectively. The random number ξ_j^t is uncorrelated in time and from one particle to another. Its distribution is flat on $[-\pi, \pi]$. The slight generalization with respect to the standard Vicsek model consists in the introduction of the parameter λ , which characterizes the probability of self-diffusion per unit time. In the original model, $\lambda \Delta t = 1$. Note that, whenever possible, we have defined the agent-based model with notations consistent with that of the binary collision model, in order to facilitate comparison between the two models.

The Vicsek model has been studied in details in the literature [12, 14, 15]. A transition towards collective motion has been reported in early studies [12], and later shown to exhibit strong finite size effects [14]. In appendix A, we recall the methodology used to study the transition, in particular the finite size scaling effects.

2.2. Dimensionless parameters

A first step in the understanding of the models is to identify the relevant dimensionless parameters and the possible regimes. Let us first consider the different length scales appearing in this problem: the interaction range d_0 , the ballistic length $\ell_{\text{bal}} = v_0/\lambda$ and the typical distance between particles $\ell_{\text{pp}} = 1/\sqrt{\rho}$. With these three different lengths, one can form the following dimensionless numbers H and B :

$$H = \frac{\ell_{\text{pp}}}{d_0} = \frac{1}{d_0\sqrt{\rho}}, \quad B = \frac{\ell_{\text{bal}}}{d_0} = \frac{v_0}{d_0\lambda}. \quad (5)$$

H characterizes whether a system is diluted ($H \gg 1$) or dense. One can see B as the relative weight of stand-alone flight over interaction. If B is large, ballistic flight is more important than collision and we can expect that particles are less correlated locally.

These numbers turn out to play an important role in the identification of the regimes of validity of the approximations we use, as seen in the following. The model also exhibits different behaviours for the different regimes which are defined by these numbers. At fixed noise intensity and fixed B , a more (resp. less) dense system is expected to move (resp. not) in a collective manner. At fixed noise and fixed dilution H , increasing B makes the flights more ballistic, which should favour collective motion. So one can guess that a relevant control parameter will be a combination of H and B (see section 4.1).

2.3. Summary of the main results

The paper is organized as follows. Section 3 is devoted to the derivation from the Boltzmann equation, through a specific approximation scheme, of the hydrodynamic equations for the continuous time binary collision model. Section 4 deals with the analysis of the phase diagram of the binary collision model, by looking at the stationary homogeneous solutions and studying their linear stability. A transition toward collective motion is observed, but the spatially homogeneous motion turns out to be unstable in the validity domain of the hydrodynamic equations, namely close to the transition line. A comparison with the agent-based model is presented, showing that the transition lines of both models are qualitatively similar and share some quantitative properties. Then, section 5 investigates the behaviour of the binary collision model beyond the strict domain of validity of the hydrodynamic equations. A direct stability analysis shows that far from the transition line, the spatially homogeneous motion is stable. We then test whether the hydrodynamic equations could be used, in this domain, as a semi-quantitative description. We find that the restabilization phenomenon is indeed observed in the hydrodynamic equations, although the predicted location of the transition line between stable and unstable motion does not match quantitatively with a perturbative treatment of the kinetic theory. We also show that there exist solitary wave solutions of the hydrodynamic equations that resemble the travelling stripes of higher density observed in the agent-based model. Finally, section 6 discusses the main conclusions and perspectives of the present work. Some technical aspects related to the agent-based model and to the stability analysis of the homogeneous motion are reported in appendix A and appendix B, respectively.

3. Boltzmann approach and hydrodynamic equations

3.1. Description in terms of Boltzmann equation

One of the main goals of this work is to derive analytically from the microscopic dynamics, within an appropriate approximation scheme, the equations governing the evolution of the hydrodynamic fields, namely the density and velocity fields. A standard approach to obtain these hydrodynamic equations is to write, as a first step, the Boltzmann equation describing the evolution of the one-particle probability distribution in phase-space (i.e. the probability that a particle is at a given point, with a given velocity), and then to derive hydrodynamic equations by computing the first moments of the Boltzmann equation. Note, however, that such a procedure often yields a hierarchy of equations, so that a closure assumption has to be used.

Let us start by deriving the Boltzmann equation for the above model. This equation relies on the standard assumption that the gas is diluted, meaning that the typical distance ℓ_{pp} between particles is large compared to the interaction distance d_0 , that is $H \gg 1$. In the present context, one also needs to assume that the ballistic distance ℓ_{bal} is much larger than d_0 , namely $B \gg 1$. It ensures that there is no memory effect from one collision to the other. The Boltzmann equation governs the evolution of the distribution $f(\mathbf{r}, \theta, t)$ that gives the probability that a particle is at point \mathbf{r} with a velocity along the direction defined by the angle θ . On general grounds, this equation can be written as

$$\frac{\partial f}{\partial t}(\mathbf{r}, \theta, t) + v_0 \mathbf{e}(\theta) \cdot \nabla f(\mathbf{r}, \theta, t) = I_{\text{dif}}[f] + I_{\text{col}}[f, f]. \quad (6)$$

The different terms in the equation can be interpreted as follows. The second term on the lhs corresponds to the ballistic motion of particles between two stochastic events (self-diffusion or collision). On the rhs, the term $I_{\text{dif}}[f]$ accounts for the self-diffusion events, and it reads

$$I_{\text{dif}}[f] = -\lambda f(\mathbf{r}, \theta, t) + \lambda \int_{-\pi}^{\pi} d\theta' \int_{-\infty}^{\infty} d\eta p_0(\eta) \sum_{m=-\infty}^{\infty} \delta(\theta' + \eta - \theta + 2m\pi) f(\mathbf{r}, \theta', t). \quad (7)$$

The sum of δ -distributions accounts for the periodicity of angles. Finally, the term $I_{\text{col}}[f, f]$ describes the effects of collisions. It can be derived in the following way. A collision between two particles occurs if their relative distance becomes less than d_0 . Although the two particles *a priori* play a symmetric role, it is convenient to choose one particle and to observe the situation in the referential of this particle—say particle 1. In this frame, the velocity of particle 2 is $\tilde{\mathbf{v}}_2 = v_0(\mathbf{e}(\theta_2) - \mathbf{e}(\theta_1))$. Hence, in order to collide with particle 1 between t and $t + dt$, particle 2 has to lie at time t (in the referential of particle 1) in a rectangle of length $|\tilde{\mathbf{v}}_2| dt$ and of width $2d_0$. Coming back to the laboratory frame, this rectangle deforms into a parallelogram, but keeps the same surface, given by $2d_0 v_0 |\mathbf{e}(\theta_2) - \mathbf{e}(\theta_1)| dt$. The collision term $I_{\text{col}}[f, f]$ is then obtained from the bilinear functional $I_{\text{col}}[g, h]$:

$$\begin{aligned} I_{\text{col}}[g, h] = & -2d_0 v_0 g(\mathbf{r}, \theta, t) \int_{-\pi}^{\pi} d\theta' |\mathbf{e}(\theta') - \mathbf{e}(\theta)| h(\mathbf{r}, \theta', t) \\ & + 2d_0 v_0 \int_{-\pi}^{\pi} d\theta_1 \int_{-\pi}^{\pi} d\theta_2 \int_{-\infty}^{\infty} d\eta p(\eta) |\mathbf{e}(\theta_2) - \mathbf{e}(\theta_1)| \\ & \times g(\mathbf{r}, \theta_1, t) h(\mathbf{r}, \theta_2, t) \sum_{m=-\infty}^{\infty} \delta(\bar{\theta} + \eta - \theta + 2m\pi), \end{aligned} \quad (8)$$

with again the notation $\bar{\theta} = \arg(e^{i\theta_1} + e^{i\theta_2})$, and where g and h are arbitrary phase-space distributions.

It is straightforward to check that the uniform one-particle distribution $f_0(\mathbf{r}, \theta, t) = \rho_0/2\pi$, associated with a uniform density of particles ρ_0 , is a stationary solution of the Boltzmann equation, for any values of the noise parameters σ and σ_0 , since each term in equation (6) vanishes independently. If a transition to a state with collective motion occurs, another distribution should be a steady-state solution of the Boltzmann equation. Yet, finding this non-trivial distribution through non-perturbative analytical method is a hard task. One could turn to numerical approaches, but we would rather like to obtain analytical results, at least in some specific regime. We thus use an alternative approach in the following, which consists in deriving hydrodynamic equations for the density and velocity fields from the Boltzmann equation, in the limit of small hydrodynamic velocity. A stability analysis can then be performed on these hydrodynamic equations in order to check the onset of collective motion.

3.2. Derivation of the hydrodynamic equations

3.2.1. Hydrodynamic fields and continuity equation. The hydrodynamic fields are on the one hand the density field:

$$\rho(\mathbf{r}, t) = \int_{-\pi}^{\pi} d\theta f(\mathbf{r}, \theta, t), \quad (9)$$

and on the other hand the velocity field:

$$\mathbf{u}(\mathbf{r}, t) = \frac{v_0}{\rho(\mathbf{r}, t)} \int_{-\pi}^{\pi} d\theta f(\mathbf{r}, \theta, t) \mathbf{e}(\theta). \quad (10)$$

The equations governing the evolution of these hydrodynamic fields are derived by taking the successive moments of the Boltzmann equation. A simple integration of equation (6) over θ directly leads the evolution equation for $\rho(\mathbf{r}, t)$:

$$\frac{\partial \rho}{\partial t} + \nabla \cdot (\rho \mathbf{u}) = 0, \quad (11)$$

which is nothing but the usual continuity equation accounting for the conservation of the number of particles.

3.2.2. Angular Fourier expansion of the phase-space distribution. The derivation of the evolution equation for the velocity field is actually much more complicated, and one has to resort to approximation schemes. As $f(\mathbf{r}, \theta, t)$ is a periodic function of θ , it is convenient to work with its Fourier series expansion, defined as

$$\hat{f}_k(\mathbf{r}, t) = \int_{-\pi}^{\pi} d\theta f(\mathbf{r}, \theta, t) e^{ik\theta}. \quad (12)$$

Conversely, $f(\mathbf{r}, \theta, t)$ can be expressed as a function of the Fourier coefficients through the relation

$$f(\mathbf{r}, \theta, t) = \frac{1}{2\pi} \sum_{k=-\infty}^{\infty} \hat{f}_k(\mathbf{r}, t) e^{-ik\theta}. \quad (13)$$

In this framework, the uniform distribution $f_0(\mathbf{r}, \theta, t) = (2\pi)^{-1}\rho_0$ corresponds to $\hat{f}_k(\mathbf{r}, t) = (2\pi)^{-1}\rho_0\delta_{k,0}$.

Let us use as a basis of the plane the two orthogonal vectors $\mathbf{e}_1 = \mathbf{e}(0)$ and $\mathbf{e}_2 = \mathbf{e}(\pi/2)$. The components of $\mathbf{e}(\theta)$ in this basis are obviously $e_1(\theta) = \cos \theta$ and $e_2(\theta) = \sin \theta$. In order

to obtain an evolution equation for the velocity field, we multiply equation (6) by $\mathbf{e}(\theta)$ and integrate over θ ; one gets in tensorial notations ($j = 1, 2$)

$$\begin{aligned} \frac{\partial}{\partial t} \int_{-\pi}^{\pi} d\theta \mathbf{e}_j(\theta) f(\mathbf{r}, \theta, t) + v_0 \sum_{l=1}^2 \frac{\partial}{\partial x_l} \int_{-\pi}^{\pi} d\theta \mathbf{e}_j(\theta) e_l(\theta) f(\mathbf{r}, \theta, t) \\ = \int_{-\pi}^{\pi} d\theta \mathbf{e}_j(\theta) (I_{\text{dif}}[f] + I_{\text{col}}[f, f]). \end{aligned} \quad (14)$$

To proceed further, it is convenient to identify complex numbers with two-dimensional vectors, in such a way that $\mathbf{e}(\theta)$ is mapped onto $e^{i\theta}$. Then, in the same way, $v_0 \hat{f}_1(\mathbf{r}, t)$ is associated with the momentum field $\mathbf{w}(\mathbf{r}, t) = \rho(\mathbf{r}, t) \mathbf{u}(\mathbf{r}, t)$. Hence, we wish to rewrite equation (14) in such complex notations. For later use, we shall write it in a slightly more general form, replacing $e^{i\theta}$ with $e^{ik\theta}$ (k being an integer):

$$\begin{aligned} \frac{\partial}{\partial t} \int_{-\pi}^{\pi} d\theta e^{ik\theta} f(\mathbf{r}, \theta, t) + v_0 \sum_{l=1}^2 \frac{\partial}{\partial x_l} \int_{-\pi}^{\pi} d\theta e^{ik\theta} e_l(\theta) f(\mathbf{r}, \theta, t) \\ = \int_{-\pi}^{\pi} d\theta e^{ik\theta} (I_{\text{dif}}[f] + I_{\text{col}}[f, f]). \end{aligned} \quad (15)$$

Equation (14) is recovered for $k = 1$, up to the mapping between complex numbers and two-dimensional vectors. The first term on the lhs is simply $\partial \hat{f}_k / \partial t$. The rhs of equation (15) is computed by inserting the Fourier series expansion (13) into equations (7) and (8). After a rather straightforward calculation, one finds

$$\begin{aligned} \int_{-\pi}^{\pi} d\theta e^{ik\theta} (I_{\text{dif}}[f] + I_{\text{col}}[f]) = -\lambda (1 - e^{-k^2 \sigma_0^2 / 2}) \hat{f}_k(\mathbf{r}, t) \\ - \frac{2}{\pi} d_0 v_0 \sum_{q=-\infty}^{\infty} (I_q - e^{-k^2 \sigma^2 / 2} I_{q-k/2}) \hat{f}_q(\mathbf{r}, t) \hat{f}_{k-q}(\mathbf{r}, t), \end{aligned} \quad (16)$$

where the coefficients I_q are defined as

$$I_q = \int_{-\pi}^{\pi} d\theta \left| \sin \frac{\theta}{2} \right| \cos q\theta. \quad (17)$$

From this definition, it is obvious that $I_{-q} = I_q$. For integer q , I_q is given by

$$I_q = \frac{4}{1 - 4q^2}, \quad (18)$$

while for the half-integer $q = m + \frac{1}{2}$ (m integer) one has

$$I_{\frac{1}{2}} = I_{-\frac{1}{2}} = 2, \quad (19)$$

$$I_{m+\frac{1}{2}} = \frac{1}{m(m+1)} [(-1)^m (2m+1) - 1], \quad m \neq -1, 0. \quad (20)$$

The second term on the lhs of equation (15) can be evaluated as follows. For $l = 1, 2$ and k integer, let us define the complex quantity $Q_l^{(k)}(\mathbf{r}, t)$ as

$$Q_l^{(k)}(\mathbf{r}, t) = \int_{-\pi}^{\pi} d\theta e^{ik\theta} e_l(\theta) f(\mathbf{r}, \theta, t). \quad (21)$$

The following relations are then easily obtained:

$$Q_1^{(k)}(\mathbf{r}, t) = \frac{1}{2} [\hat{f}_{k+1}(\mathbf{r}, t) + \hat{f}_{k-1}(\mathbf{r}, t)], \quad (22)$$

$$Q_2^{(k)}(\mathbf{r}, t) = \frac{1}{2i} [\hat{f}_{k+1}(\mathbf{r}, t) - \hat{f}_{k-1}(\mathbf{r}, t)]. \quad (23)$$

3.2.3. Velocity field equation in the small velocity regime. Up to now, the calculations made are exact, apart from the approximations underlying the Boltzmann equation. As already mentioned, the Fourier coefficient $\hat{f}_0(\mathbf{r}, t)$ is nothing but the density field $\rho(\mathbf{r}, t)$, and $\hat{f}_1(\mathbf{r}, t)$ can be mapped onto the momentum field $\mathbf{w}(\mathbf{r}, t)$ through the identification of complex numbers with two-dimensional vectors. A similar mapping also holds for $\hat{f}_{-1}(\mathbf{r}, t)$, which is the complex conjugate of $\hat{f}_1(\mathbf{r}, t)$. In contrast, Fourier coefficient $\hat{f}_k(\mathbf{r}, t)$ with $|k| > 1$ cannot be mapped onto the hydrodynamic fields. As it turns out that such coefficients appear both in the expression of $Q_l^{(k)}(\mathbf{r}, t)$ and on the rhs of equation (15), an approximation scheme has to be found in order to obtain from equation (15) a closed hydrodynamic equation, involving only the fields $\rho(\mathbf{r}, t)$ and $\mathbf{u}(\mathbf{r}, t)$.

In the following, we assume that the distribution $f(\mathbf{r}, \theta, t)$ is close to an isotropic distribution, namely it depends only slightly on θ . This amounts to assuming that the hydrodynamic velocity is much smaller than the velocity of individual particles. In terms of Fourier coefficients, the hydrodynamic velocity is given by $\|\mathbf{u}(\mathbf{r}, t)\| = v_0 |\hat{f}_1(\mathbf{r}, t)| / \rho(\mathbf{r}, t)$. We introduce a small parameter ϵ such that $\|\mathbf{u}(\mathbf{r}, t)\| = \mathcal{O}(\epsilon)$. For instance, ϵ can be chosen as \bar{u}/v_0 , where \bar{u} is the spatial average of $\|\mathbf{u}(\mathbf{r}, t)\|$ at some initial time $t = t_0$. Then the key assumption we use to build an approximation scheme is

$$\hat{f}_k(\mathbf{r}, t) = \mathcal{O}(\epsilon^{|k|}). \quad (24)$$

Such a scaling ansatz is consistent with the property $\hat{f}_{-k}(\mathbf{r}, t) = \hat{f}_k(\mathbf{r}, t)^*$, with the scaling properties of $\hat{f}_0(\mathbf{r}, t)$ and $\hat{f}_1(\mathbf{r}, t)$, and with equation (16). We shall identify more precisely in section 4.1.2 the validity domain of this scaling ansatz, and thus of the hydrodynamic equations we will derive from it.

Using the above scaling ansatz, the sum on the rhs of equation (16), for $k = 1$, can be truncated, only keeping terms with $q = 0, 1$ or 2 , that are at most of order ϵ^3 , while discarding the other terms, being of higher order in ϵ . Gathering all terms, one obtains the following equation for the evolution of \hat{f}_1 (we drop the explicit dependence upon \mathbf{r} and t to simplify the notations):

$$\begin{aligned} \frac{\partial \hat{f}_1}{\partial t} + \frac{v_0}{2} \frac{\partial}{\partial x_1} (\hat{f}_2 + \rho) + \frac{v_0}{2i} \frac{\partial}{\partial x_2} (\hat{f}_2 - \rho) = & - \left[\lambda(1 - e^{-\sigma_0^2/2}) + \frac{8}{\pi} d_0 v_0 \left(\frac{2}{3} - e^{-\sigma^2/2} \right) \rho \right] \hat{f}_1 \\ & - \frac{8}{\pi} d_0 v_0 \left(e^{-\sigma^2/2} - \frac{2}{5} \right) \hat{f}_1^* \hat{f}_2. \end{aligned} \quad (25)$$

Hence, the resulting equation involves $\hat{f}_0 = \rho$, \hat{f}_1 and \hat{f}_2 . Accordingly, it turns out that one needs to find a closure relation to express \hat{f}_2 as a function of \hat{f}_0 and \hat{f}_1 (or, equivalently, in terms of ρ and \mathbf{u}). Such a relation is given by the evolution equation for \hat{f}_2 , that is, equation (15) with $k = 2$. From equation (16), one sees that Fourier coefficients \hat{f}_q with $|q| > 2$ are *a priori* involved, but they can actually be discarded as being of order higher than ϵ^2 , whereas $\hat{f}_2 = \mathcal{O}(\epsilon^2)$. Similarly, the quantity $Q_l^{(2)}$ can be expressed as a function of \hat{f}_1 and \hat{f}_3 , and here again, \hat{f}_3 can be neglected. One thus ends up with the following equation for \hat{f}_2 :

$$\begin{aligned} \frac{\partial \hat{f}_2}{\partial t} + \frac{v_0}{2} \frac{\partial \hat{f}_1}{\partial x_1} - \frac{v_0}{2i} \frac{\partial \hat{f}_1}{\partial x_2} = & - \left[\lambda(1 - e^{-2\sigma_0^2}) + \frac{16}{3\pi} d_0 v_0 \left(\frac{7}{5} + e^{-2\sigma^2} \right) \rho \right] \hat{f}_2 \\ & + \frac{8}{\pi} d_0 v_0 \left(\frac{1}{3} + e^{-2\sigma^2} \right) \hat{f}_1^2. \end{aligned} \quad (26)$$

Within our hydrodynamic description, it is also natural to assume that the phase-space probability density $f(\mathbf{r}, \theta, t)$, or equivalently its Fourier coefficients $\hat{f}_k(\mathbf{r}, t)$, varies significantly only over time and length scales that are much larger than the microscopic

ones. Relevant microscopic time scales are the typical collision time $\tau_{\text{col}} = 1/(\rho d_0 v_0)$ and the typical ballistic time $\tau_{\text{bal}} = 1/\lambda$ between self-diffusion events. It is thus legitimate to neglect the term $\partial \hat{f}_2 / \partial t$ in equation (26), as it is much smaller than $\hat{f}_2 / \tau_{\text{col}}$ and $\hat{f}_2 / \tau_{\text{bal}}$. In contrast, the terms containing the spatial derivatives have to be retained, as they involve \hat{f}_1 which is much larger than \hat{f}_2 .

From equation (26)—without the time-derivative term—one can express \hat{f}_2 as a function of ρ and \hat{f}_1 . Then plugging this expression for \hat{f}_2 into equation (15), with $k = 1$, leads to a closed hydrodynamic equation governing the evolution of \hat{f}_1 , and involving only \hat{f}_1 and ρ . Mapping back complex numbers onto two-dimensional vectors, $v_0 \hat{f}_1$ can be identified with the ‘momentum’ field $\mathbf{w} = \rho \mathbf{u}$, and one obtains the following hydrodynamic equation:

$$\begin{aligned} \frac{\partial \mathbf{w}}{\partial t} + \gamma (\mathbf{w} \cdot \nabla) \mathbf{w} = & -\frac{v_0^2}{2} \nabla \rho + \frac{\kappa}{2} \nabla \mathbf{w}^2 + (\mu - \xi \mathbf{w}^2) \mathbf{w} + \nu \nabla^2 \mathbf{w} \\ & - \kappa (\nabla \cdot \mathbf{w}) \mathbf{w} + 2\nu' \nabla \rho \cdot \mathbf{M} - \nu' (\nabla \cdot \mathbf{w}) \nabla \rho, \end{aligned} \quad (27)$$

with $\nu' = \partial \nu / \partial \rho$ and where $\mathbf{M} = \frac{1}{2}(\nabla \mathbf{w} + \nabla \mathbf{w}^T)$ is the symmetric part of the momentum gradient tensor. The different coefficients appearing in this equation are given by

$$\nu = \frac{v_0^2}{4} \left[\lambda (1 - e^{-2\sigma_0^2}) + \frac{16}{3\pi} d_0 v_0 \rho \left(\frac{7}{5} + e^{-2\sigma^2} \right) \right]^{-1}, \quad (28)$$

$$\gamma = \frac{16\nu d_0}{\pi v_0} \left(\frac{16}{15} + 2e^{-2\sigma^2} - e^{-\sigma^2/2} \right), \quad (29)$$

$$\kappa = \frac{16\nu d_0}{\pi v_0} \left(\frac{4}{15} + 2e^{-2\sigma^2} + e^{-\sigma^2/2} \right), \quad (30)$$

$$\mu = \frac{8}{\pi} d_0 v_0 \rho \left(e^{-\sigma^2/2} - \frac{2}{3} \right) - \lambda (1 - e^{-\sigma_0^2/2}), \quad (31)$$

$$\xi = \frac{256\nu d_0^2}{\pi^2 v_0^2} \left(e^{-\sigma^2/2} - \frac{2}{5} \right) \left(\frac{1}{3} + e^{-2\sigma^2} \right). \quad (32)$$

Equation (27) may be considered as a generalization of the Navier–Stokes equation to a case where on the one hand, the global momentum of the assembly of particles is not conserved by the microscopic dynamics and on the other hand, the dynamics breaks the Galilean invariance. This shows up in the appearance of new terms in the equation, as well as in the presence of the coefficient γ , generically different from the Navier–Stokes value $1/\rho$, in front of the $(\mathbf{w} \cdot \nabla) \mathbf{w}$ term. For instance, if $\lambda \ll \rho d_0 v_0$, $\gamma \rho$ remains close to 0.6 for any value of σ .

The different terms on the rhs of equation (27) may be interpreted as follows. Neglecting the density dependence of κ , the first two terms can be considered as a pressure gradient, where the effective pressure P_{eff} obeys the equation of state $P_{\text{eff}} = \frac{1}{2}(v_0^2 \rho - \kappa \mathbf{w}^2)$. The third term accounts for the local relaxation of the momentum field \mathbf{w} , and this term plays an important role in the onset of a collective behaviour, as we shall see in the following section (note that $\xi > 0$ when $\mu > 0$). The fourth term describes the viscous damping, like in the usual Navier–Stokes equation. The parameter ν can thus be interpreted as a kinematic viscosity. It decreases when ρ increases, but the ‘dynamic’ viscosity $\rho \nu$ increases with ρ . The fifth term may be thought of as a nonlinear feedback on the momentum field of the compressibility of the flow. Finally, the two last terms correspond to a coupling between the density and momentum gradients.

It is also important to note that the above hydrodynamic equation (27) is consistent with the phenomenological equation postulated by Toner and Tu on the basis of symmetry

considerations [17]. Specifically, expanding the expression of $\mathbf{w} = \rho \mathbf{u}$ in that equation, we find the same terms involving the velocity gradients as in [17]. But it turns out that the term $\nabla(\nabla \cdot \mathbf{w})$, which would be allowed from symmetry considerations, does not appear in the present approach, that is, the coefficient in front of it vanishes. Note also that the term $(\mathbf{u} \cdot \nabla)^2 \mathbf{u}$ considered by Toner and Tu [17] does not appear here for being of higher order than the terms retained in the expansion. Last, hydrodynamic equations which have been derived through the kinetic approach are entirely deterministic, while Toner and Tu studied stochastic equations. However, some additional terms also appear, like the coupling terms between density and velocity gradients. Most importantly, the present approach provides a microscopic justification to the hydrodynamic equation of motion and yields explicit expressions, as a function of the microscopic parameters, for the different coefficients appearing in the equations (transport coefficients).

4. Noise-density phase diagram from the hydrodynamic equations

4.1. Spatially homogeneous stationary solutions

4.1.1. Transition towards collective motion. Now that the hydrodynamic equations of motion have been derived, it is natural to look for the different possible stationary solutions and to test their stability. Let us first look for the spatially homogeneous stationary solutions. Dropping all space and time derivatives, one ends up with the simple equation

$$(\mu - \xi \mathbf{w}^2) \mathbf{w} = 0. \quad (33)$$

Hence a trivial homogeneous stationary solution is $\mathbf{w} = 0$ for all values of the parameters. When $\mu > 0$, a second solution appears, namely $\mathbf{w} = \mathbf{w}_1 = \sqrt{\mu/\xi} \mathbf{e}$, where \mathbf{e} is a unit vector pointing in an arbitrary direction. The stability against spatially homogeneous perturbations is easily tested by assuming that the flow is homogeneous, but time-dependent in equation (27), yielding

$$\frac{\partial \mathbf{w}}{\partial t} = (\mu - \xi \mathbf{w}^2) \mathbf{w}. \quad (34)$$

It follows that $\mathbf{w} = 0$ is a stable solution when $\mu < 0$, while it becomes unstable for $\mu > 0$. In the latter case, the emerging solution $\mathbf{w} = \mathbf{w}_1$ is stable against homogeneous perturbations. From the expression (31) of μ , we see that the sign of μ is related to a competition between density and self-diffusion. When the self-diffusion probability λ is high, $\mu < 0$ and there is no flow. In contrast, when the density is high, $\mu > 0$ and a spontaneous flow appears due to the numerous interactions between particles. The value $\mu = 0$ defines a transition line in the phase diagram noise versus density: for given values σ and σ_0 of the noises, the nonzero solution $\mathbf{w} = \mathbf{w}_1$ appears for a density $\rho > \rho_t$, where the threshold density ρ_t is given by

$$\rho_t = \frac{\pi \lambda (1 - e^{-\sigma_0^2/2})}{8 d_0 v_0 (e^{-\sigma^2/2} - \frac{2}{3})}. \quad (35)$$

In terms of the dimensionless parameter (or reduced density)

$$p = \frac{B}{H^2} = \frac{d_0 \ell_{\text{bal}}}{\ell_{\text{pp}}^2} = \frac{\rho d_0 v_0}{\lambda}, \quad (36)$$

the threshold is expressed as

$$p_t = \frac{\pi (1 - e^{-\sigma_0^2/2})}{8 (e^{-\sigma^2/2} - \frac{2}{3})}. \quad (37)$$

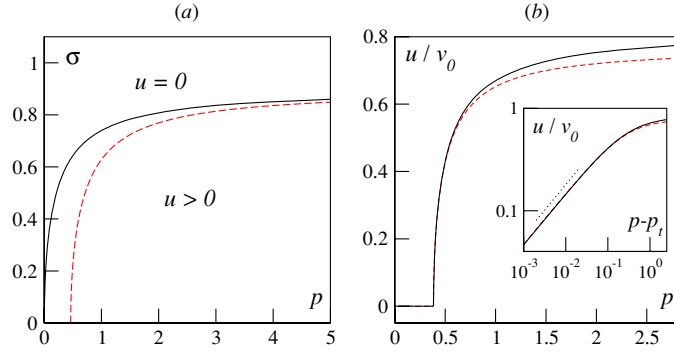


Figure 1. (a) Phase diagram of the model in the plane (p, σ) , with $p = \rho v_0 d_0 / \lambda$. A transition line (full line: $\sigma_0 = \sigma$; dashed line: $\sigma_0 = 1$) indicates the linear instability threshold of the state $u = |\mathbf{u}| = 0$. (b) Hydrodynamic velocity u in the homogeneous state for $\sigma = \sigma_0 = 0.6$, computed numerically from the Boltzmann equation (full line) and analytically from the hydrodynamic equations (dashed line). Inset: same data on logarithmic scales (dots: slope $1/2$).

This last result is interesting, as it shows that the threshold p_t , which could *a priori* depend on the three dimensionless numbers σ , σ_0 and B , actually does not depend on B . The transition line is plotted in figure 1(a) for the two cases $\sigma_0 = \sigma$ and $\sigma_0 = 1$. Instead of considering the transition as a function of the density, one may also look for the transition by varying the noises at a given fixed density. If the two noise intensities σ_0 and σ are equal, the instability of $\mathbf{w} = 0$ occurs for any (non-zero) density, and the threshold noise σ_t behaves in the low density limit $p \rightarrow 0$ as $\sigma_t \sim p^{1/2}$. This nontrivial prediction can be verified in direct numerical simulations (see below). In contrast, when σ_0 is kept fixed while varying σ , no transition occurs as a function of σ if the reduced density is lower than a limit p_t^0 given by

$$p_t^0 = \frac{3\pi}{8} (1 - e^{-\sigma_0^2/2}). \quad (38)$$

Finally, in the opposite limit of high density, the threshold noise σ_t saturates to a value $\sigma_t^\infty = (2 \ln \frac{3}{2})^{1/2} \approx 0.90$.

4.1.2. Validity domain of the hydrodynamic equations. The hydrodynamic equations rely on the scaling ansatz (24). In order to verify *a posteriori* the validity of the hydrodynamic equations, we compare the stationary homogeneous solutions with non-zero velocity obtained from the hydrodynamic equations to that numerically computed from the Boltzmann equation. The hydrodynamic velocity u , computed as $u = u_1 \equiv \rho^{-1} \sqrt{\mu/\xi}$, is plotted in figure 1(b) as a function of the reduced density p . Note that u/v_0 is a function of the dimensionless numbers p , σ and σ_0 only. As expected, the velocity u computed from the hydrodynamic equation matches perfectly, in the small velocity regime (i.e. close to the transition line), the numerical data from the Boltzmann equation. However, it turns out that even quite far from the transition, when u becomes of the order of v_0 , the value u_1 computed from the hydrodynamic equation remains a good estimate of the value obtained from the Boltzmann equation. In particular, it is interesting to note that u_1 also saturates at large ρ to a finite value $u_1^\infty(\sigma) < 1$, given by

$$u_1^\infty(\sigma) = v_0 \left[\frac{2(e^{-\sigma^2/2} - \frac{2}{3})(\frac{7}{15} + \frac{1}{3}e^{-2\sigma^2})}{(e^{-\sigma^2/2} - \frac{2}{3})(\frac{1}{3} + e^{-2\sigma^2})} \right]^{\frac{1}{2}} \quad (39)$$

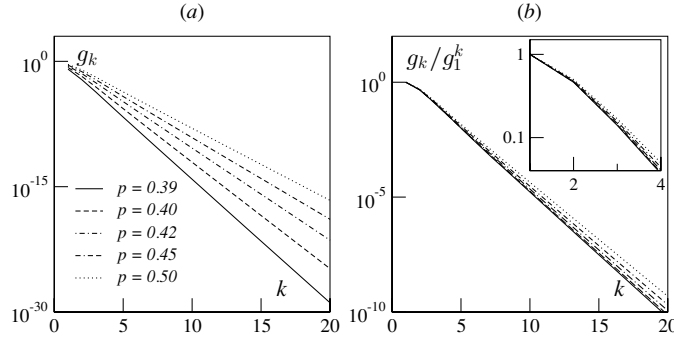


Figure 2. Test of the scaling ansatz $\hat{f}_k = \mathcal{O}(\epsilon^{|k|})$. (a) $g_k = \hat{f}_k^{\text{st}}/\rho$ versus k , for $\sigma = \sigma_0 = 0.6$ and different values of the reduced density p , close to the transition density ($p_t = 0.3837$); an exponential decay is observed. (b) g_k/g_1^k as a function of k , showing that for a given k , g_k is essentially proportional to g_1^k when the density is varied ($\lambda = 0.5, d_0 = 0.5, v_0 = 1$). Inset: zoom on the small k region.

(see figure 1(b)). Hence, even beyond their domain of validity, which is restricted to small values of the hydrodynamic velocity, the hydrodynamic equations we have derived yield a rather good approximation of the exact dynamics. Specifically, they fulfil the condition that the hydrodynamic velocity should remain smaller than the individual velocity v_0 of the particles, although this result was not *a priori* obvious given the approximations made.

To further test the validity of the hydrodynamic equations, we have also checked explicitly, from a numerical calculation, that the scaling ansatz (24) is correct. Specifically, we computed from a numerical integration the stationary and spatially homogeneous solution \hat{f}_k^{st} of the Boltzmann equation. In order to work with dimensionless quantities, we plot in figure 2(a) the quantities $g_k = \hat{f}_k^{\text{st}}/\rho$ (instead of \hat{f}_k^{st}) as a function of k . We observe that g_k decays almost exponentially with k , as soon as $k \gtrsim 4$. To test the scaling ansatz, we first reformulate it in a more specific way. The ansatz is obeyed if there exists for all k a constant c_k such that $g_k \approx c_k g_1^k$ in a parameter regime where $g_1 \ll 1$. We thus plot on figure 2(b) the ratio g_k/g_1^k for different values of the density, close to the transition, and we observe a reasonable collapse of the data. Let us, however, emphasize that a strict collapse of the data is not necessary in order to apply the approximation scheme used in the derivation of the hydrodynamic equations. The essential requirement is that the quantities g_k with $k > 2$ could be neglected. As the ratio g_k/g_1^k decays rapidly with k , neglecting terms with $k > 2$ is a safe approximation.

4.2. Stability against inhomogeneous perturbations of the homogeneous stationary solutions

4.2.1. Evolution equation for the perturbations. We have shown that above a threshold density ρ_t , or equivalently below a threshold noise σ_t , the solution with zero velocity becomes unstable, and a stable solution with finite velocity emerges. Yet, only the stability with respect to homogeneous perturbations (i.e. with infinite wavelength) has been tested up to now. Hence this does not ensure that the finite velocity solution is really stable, as it may be destabilized by finite wavelength perturbations. We now check this issue, by introducing small perturbations around the homogeneous stationary solutions ρ_0 and \mathbf{w}_0 , namely

$$\rho(\mathbf{r}, t) = \rho_0 + \delta\rho(\mathbf{r}, t), \quad \mathbf{w}(\mathbf{r}, t) = \mathbf{w}_0 + \delta\mathbf{w}(\mathbf{r}, t). \quad (40)$$

Note that \mathbf{w}_0 may either be equal to zero or to the nonzero solution \mathbf{w}_1 . Plugging these expressions into the hydrodynamic equations (11) and (27), we can expand the resulting

equations to the first order in the perturbation fields $\delta\rho(\mathbf{r}, t)$ and $\delta\mathbf{w}(\mathbf{r}, t)$, also taking into account the density dependence of the different coefficients. This yields the following linearized equations:

$$\frac{\partial}{\partial t}\delta\rho + \nabla \cdot \delta\mathbf{w} = 0, \quad (41)$$

$$\begin{aligned} \frac{\partial}{\partial t}\delta\mathbf{w} + \gamma(\mathbf{w}_0 \cdot \nabla)\delta\mathbf{w} = & -\frac{v_0^2}{2}\nabla\delta\rho + \kappa\nabla(\mathbf{w}_0 \cdot \delta\mathbf{w}) \\ & + [(\mu' - \xi'\mathbf{w}_0^2)\delta\rho - 2\xi\mathbf{w}_0 \cdot \delta\mathbf{w} - \kappa\nabla \cdot \delta\mathbf{w}]\mathbf{w}_0 \\ & + (\mu - \xi\mathbf{w}_0^2)\delta\mathbf{w} + \nu\nabla^2\delta\mathbf{w}, \end{aligned} \quad (42)$$

where μ' and ξ' are shorthand notations for $\partial\mu/\partial\rho$ and $\partial\xi/\partial\rho$. Note that $\partial\mu/\partial\rho$ is actually a constant, i.e. it is independent of ρ . Then we make the following ansatz:

$$\delta\rho(\mathbf{r}, t) = \delta\rho_0 e^{st+i\mathbf{q}\cdot\mathbf{r}}, \quad \delta\mathbf{w}(\mathbf{r}, t) = \delta\mathbf{w}_0 e^{st+i\mathbf{q}\cdot\mathbf{r}}, \quad (43)$$

where $\delta\mathbf{w}_0$ is a vector (with real components), and $\delta\rho_0$ is a complex amplitude that takes into account a possible phase shift between density and momentum perturbation fields. Both $\|\delta\mathbf{w}_0\|$ and $|\delta\rho_0|$ are assumed to be small. The wavenumber \mathbf{q} is assumed to have real components, whereas the growth rate s is *a priori* complex. In addition, \mathbf{q} is considered to be given, and one looks for the dispersion relation $s(\mathbf{q})$. If the real part $\Re[s(\mathbf{q})] > 0$, the mode with wavenumber \mathbf{q} is unstable. Then equations (41) and (42) become:

$$s\delta\rho_0 + i\mathbf{q} \cdot \delta\mathbf{w}_0 = 0, \quad (44)$$

$$\begin{aligned} [s + \gamma(\mathbf{w}_0 \cdot i\mathbf{q}) - (\mu - \xi\mathbf{w}_0^2) + \nu\mathbf{q}^2]\delta\mathbf{w}_0 = & -\frac{1}{2}(v_0^2\delta\rho_0 - 2\kappa\mathbf{w}_0 \cdot \delta\mathbf{w}_0)i\mathbf{q} \\ & + [(\mu' - \xi'\mathbf{w}_0^2)\delta\rho_0 - (2\xi\mathbf{w}_0 + \kappa i\mathbf{q}) \cdot \delta\mathbf{w}_0]\mathbf{w}_0. \end{aligned} \quad (45)$$

Note that, due to linearity, the above equations can be re-expressed as a function of the ratio of amplitudes $\delta\mathbf{w}_0/\delta\rho_0$.

4.2.2. Stability of the zero-velocity solution. Let us first check the stability against inhomogeneous perturbations of the solution $\mathbf{w}_0 = 0$, which is known to be stable against homogeneous perturbations in the low density phase $\rho < \rho_t$ (corresponding to $\mu < 0$). In this case, equation (45) simplifies to

$$(s + \nu\mathbf{q}^2 - \mu)\delta\mathbf{w}_0 = -\frac{i}{2}v_0^2\delta\rho_0\mathbf{q}. \quad (46)$$

Thus $\delta\mathbf{w}_0$ is along the same direction as \mathbf{q} . Writing $\mathbf{q} = q\mathbf{e}$ and $\delta\mathbf{w}_0 = \delta w_0\mathbf{e}$, where \mathbf{e} is an arbitrary unit vector, one can eliminate the ratio $\delta w_0/\delta\rho_0$ from equation (44), yielding

$$s^2 + (\nu q^2 - \mu)s + \frac{v_0^2}{2}q^2 = 0. \quad (47)$$

The discriminant of this second-order polynomial equation reads (note that $\mu < 0$)

$$\Delta = (|\mu| + \nu q^2)^2 - 2v_0^2q^2. \quad (48)$$

If $\Delta \geq 0$, the roots are real, and one finds for the largest one s_+ :

$$s_+ = \frac{1}{2}[-(|\mu| + \nu q^2) + \sqrt{(|\mu| + \nu q^2)^2 - 2v_0^2q^2}] < 0. \quad (49)$$

In the opposite case $\Delta < 0$, the roots s_{\pm} are complex conjugates, and their real part is given by

$$\Re[s_{\pm}] = -\frac{1}{2}(|\mu| + \nu q^2) < 0. \quad (50)$$

As a consequence, the homogeneous fields $\mathbf{w}_0 = 0$ is stable with respect to finite wavelength perturbations in the region $\rho < \rho_t$.

4.2.3. Stability of homogeneous collective motion. We now turn to the stability analysis of the stationary homogeneous flow $\mathbf{w}_0 = \mathbf{w}_1$, obtained for $p > p_t$. For the hydrodynamic equations to be valid, we restrict our study to values of p very close to p_t , with $p > p_t$. One could *a priori* consider vectors \mathbf{q} and $\delta\mathbf{w}_0$ that make arbitrary angles with respect to \mathbf{w}_1 . However, it can be shown (see appendix B) that only some specific angles are allowed. Further, for all allowed perturbation modes such that \mathbf{q} and $\delta\mathbf{w}_0$ are not along the direction of \mathbf{w}_1 , the real part of the growth rate s is negative, so that these modes are stable (appendix B). The only instability that appears is for longitudinal perturbations, such that \mathbf{q} , $\delta\mathbf{w}_0$ and \mathbf{w}_1 all have the same direction. We thus focus on this specific case in the following.

Considering a longitudinal perturbation, we write $\mathbf{w}_1 = w_1\mathbf{e}$, $\mathbf{q} = q\mathbf{e}$ and $\delta\mathbf{w}_0 = \delta w_0\mathbf{e}$, where \mathbf{e} is a unit vector. Under these assumptions, equations (44) and (45) become

$$s\delta\rho_0 + iq\delta w_0 = 0, \quad (51)$$

$$(s + \gamma iq w_1 + vq^2)\delta w_0 = -\frac{iq}{2}(v_0^2\delta\rho_0 - 2\kappa w_1\delta w_0) + w_1[(\mu' - \xi' w_1^2)\delta\rho_0 - (2\xi w_1 + iq\kappa)\delta w_0], \quad (52)$$

where we also take into account that $\mu - \xi w_1^2 = 0$. From equation (51), one gets $\delta w_0/\delta\rho_0 = -s/iq$, which we report in equation (52). This yields a polynomial of second degree in s :

$$s^2 + s[(vq^2 + 2\mu) + iq\gamma w_1] + \left[\frac{q^2 v_0^2}{2} + iq w_1(\mu' - \xi' w_1^2)\right] = 0, \quad (53)$$

from which two solutions s_{\pm} can be obtained. Denoting as s_+ the solution with the largest real part, we find

$$\Re[s_+] = -\frac{1}{2}(vq^2 + 2\mu) + \sqrt{\frac{1}{8}(J_1 + \sqrt{J_1^2 + J_2^2})}, \quad (54)$$

with

$$J_1 = (vq^2 + 2\mu)^2 - q^2(\gamma^2 w_1^2 + 2v_0^2) \\ J_2 = 2w_1 q[\gamma(vq^2 + 2\mu) - 2\mu' + 2\xi' w_1^2].$$

To deal with this complicated expression, we first plot $\Re[s_+]$ as a function of q for some specific values of the parameters (see figure 3(a)). Near the threshold p_t of collective motion, there exists a threshold value q_i such that $\Re[s_+]$ is positive for $q < q_i$ and negative for $q > q_i$. Hence the homogeneous flow turns out to be unstable with respect to long wavelength perturbations.

This result is confirmed by a small q expansion of equation (54). Expanding $\Re[s_+]$ up to the second non-trivial order in q , that is to order q^4 since only even powers of iq appear in the expansion of the real part of s_+ , we get⁴

$$\Re[s_+] = \frac{\mu'^2}{8\xi\mu^2}q^2 - \frac{5\mu'^4}{128\xi^2\mu^5}q^4 + \mathcal{O}(q^6). \quad (55)$$

The positivity of the coefficient of the q^2 term confirms that, close to the transition line, long wavelength modes are unstable. Note that the expansion (55) is consistent as long as the

⁴ To simplify the resulting expressions, we approximate the coefficients of the expansion in q by their leading order in $1/\mu$, as μ is small close to the transition line. The full expression of the coefficient s_2 of the q^2 term reads

$$s_2 = \frac{1}{8} \left[\frac{1}{\xi} \left(\frac{\mu'}{\mu} - \frac{\xi'}{\xi} - \gamma \right)^2 - \frac{\gamma^2}{\xi} - \frac{2v_0^2}{\mu} \right].$$

This expression will be used in figure 5 to compare with numerical results.

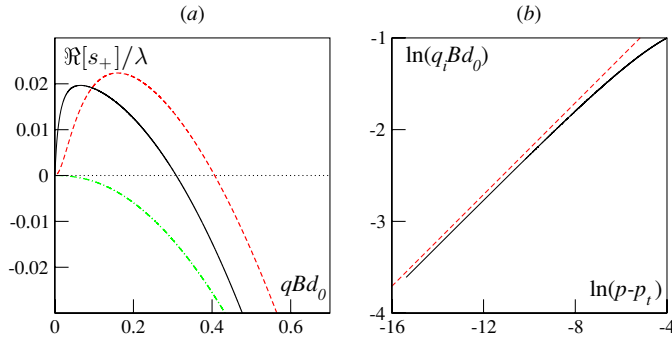


Figure 3. Longitudinal instability. (a) $\Re[s_+]/\lambda$ versus q for $p = 0.22$ (full line), 0.30 (dashed) and $p = 0.4$ (dot-dashed), and $\sigma = \sigma_0 = 0.5$ ($p_t = 0.2138$). (b) $(q_i B d_0)$ versus $(p - p_t)$ in logarithmic scales. The dashed line indicates the scaling $q_i \propto (p - p_t)^{1/4}$.

fourth-order term remains small with respect to the second-order one, yielding the condition $q \ll q^*$ which defines the wavenumber q^* :

$$q^* = d_0^{-1} B^{-1} (p - p_t)^{3/2} \Psi(p). \quad (56)$$

The function $\Psi(p)$ goes to a constant value for $p \rightarrow 0$, and $\Psi(p) \sim p^{-1/2}$ for $p \rightarrow \infty$. The wave vector q^* defines the region where the first term of the expansion of $\Re[s_+]$ is dominant.

Interestingly, we observe that other wavenumbers characterizing $\Re[s_+]$ have a different scaling with $p - p_t$, the deviation from the threshold. For instance, it can be shown analytically that the wavenumber q_i , defined by $\Re[s_+] = 0$, scales as $q_i \sim w_1^{1/2} \sim (p - p_t)^{1/4}$, as illustrated in figure 3(b). The wavenumber q_i delimitates the domain of unstable modes. Another example is given by the wavenumber q_m that maximizes $\Re[s_+]$ and thus corresponds to the most unstable modes: q_m is found to scale as $q_m \sim w_1 \sim (p - p_t)^{1/2}$. The existence of these different scaling regimes is an illustration of the complexity of the dynamics close to the transition line.

Finally, we emphasize that the perturbations that destabilize the homogeneous collective motion (that is, the long-range order) are different from the ones that destabilize long-range order in the XY-model, an equilibrium model with essentially the same symmetries as in the present model. In our model, motion is destabilized by longitudinal waves, while in the XY-model, long-range order is destabilized by spin-waves, that is by a small change in the spin direction from one spin to the neighbouring ones.

4.3. Comparison with the phase diagram of the agent-based model

4.3.1. Numerics and parameters. All simulations are performed using models defined on a square domain, with periodic conditions on both boundaries. The initial conditions always consist of randomly dispersed particles, with a uniformly chosen random speed direction. Then all measurements are performed after a sufficiently long time so that a stationary state is reached.

In the above framework of the Boltzmann equation, we considered diluted systems with small correlations between particles, which is expressed in terms of the dimensionless number H and B as

$$H \gg 1, \quad B \gg 1. \quad (57)$$

In the numerical agent-based model, we do not have access to very large values of H and B , due to simulation constraints. However, to be as consistent as possible with the kinetic theory

Table 1. Physical parameters of agent-based simulations; set I corresponds to the values used in [15]. Parameters are chosen as a multiple or sub-multiple of 2; $\sigma_0^{\max} = \pi/\sqrt{3}$ corresponds to the same variance as a uniform noise on $[-\pi; \pi]$.

Set of parameters	σ_0	d_0	v_0	λ	ρ	p	B
I	σ	1	2^{-1}	1	$[2^{-7}; 2^2]$	$[2^{-6}; 2]$	2^{-1}
II	σ	1	2^{-1}	2^{-3}	$[2^{-9}; 2^{-4}]$	$[2^{-7}; 2^{-2}]$	2^2
III	σ	1	2^{-1}	2^{-4}	$[2^{-10}; 2^{-4}]$	$[2^{-7}; 2^{-1}]$	2^3
IV	σ	1	2^{-1}	2^{-5}	$[2^{-11}; 2^{-4}]$	$[2^{-7}; 1]$	2^4
V	σ	1	1	2^{-5}	$[2^{-10}; 2^{-6}]$	$[2^{-7}; 2^{-3}]$	2^5
VI	σ	2^{-1}	2^{-1}	2^{-5}	$[2^{-11}; 2^{-5}]$	$[2^{-8}; 2^{-2}]$	2^5
VII	σ	2^{-2}	2^{-1}	2^{-5}	$[2^{-11}; 2^{-4}]$	$[2^{-9}; 2^{-2}]$	2^6
VIII	σ_0^{\max}	2^{-2}	2^{-1}	2^{-5}	$[2^{-12}; 2^{-5}]$	$[2^{-10}; 2^{-2}]$	2^6

approach, we mainly explored a parameter range such that $H \geq 4$ and $B \geq 4$. Among the three dependent dimensionless numbers B , H and p , we decided to keep B to characterize the set of parameters, and p as the control parameter.

Throughout the study, we fix $\Delta t = 1$. We defined some sets of parameters (d_0, v_0, λ) and, for each of them, we studied the behaviour of the system in the parameter space (ρ, η) . To make the comparison between analytical and numerical results easier, we characterize the noise amplitude by its rms-value σ (or equivalently its variance σ^2). For a uniform noise on the interval $[-\eta\pi, \eta\pi]$, we have $\sigma = \eta \cdot \pi/\sqrt{3}$. The self-diffusion noise is kept equal to the collision noise ($\sigma_0 = \sigma$), except for one set of parameters in which the angle of diffusion $\eta_0 \xi_j^t$ is chosen over the whole circle. We call its rms-value σ_0^{\max} . All the parameter values are summarized in table 1.

4.3.2. Transition line. When the noise amplitudes for collision and self-diffusion are equal, the general aspect of the phase diagram is the same for both the kinetic theory and the agent-based model (figure 4(a)). We have drawn the transition line for different sets of parameters in figure 4(b). All curves seem to be bounded between configurations I ($B = 0.5$) and II ($B = 4$).

Looking at the influence of the different parameters, we can make the following observations. First, there are small variations as the self-diffusion probability λ changes with a factor of 8 from configurations II–IV (figure 4(b)). When the dimensionless parameter B is kept constant (sets V and VI), the transition points corresponding to the same value of p are equal within the error bars. Apart from set I for which $B < 1$, it turns out that the measured values of σ_t differ by less than 15% for any given p , while B is varied by a factor of 16 between set II ($B = 4$) and set VII ($B = 64$). However, we are not able to conclude that the curves merge into a single master curve. In particular, the observed evolution of σ_t when increasing B at fixed p is not monotonous (figure 4(b)).

In the low p region, the transition noise varies as a power law with p , $\sigma \propto p^\beta$ when $p \rightarrow 0$. We have measured the exponent β for the largest dimensionless number B ($B = 64$, set VII), yielding $\beta = 0.46 \pm 0.04$ (figure 4(c)). This value is compatible with a square-root behaviour as found analytically in the binary collision model (figure 1). Quantitatively, the transition lines computed from the kinetic theory and the ones which we measure in the agent-based model are relatively close to each other; their largest relative difference is about 30%.

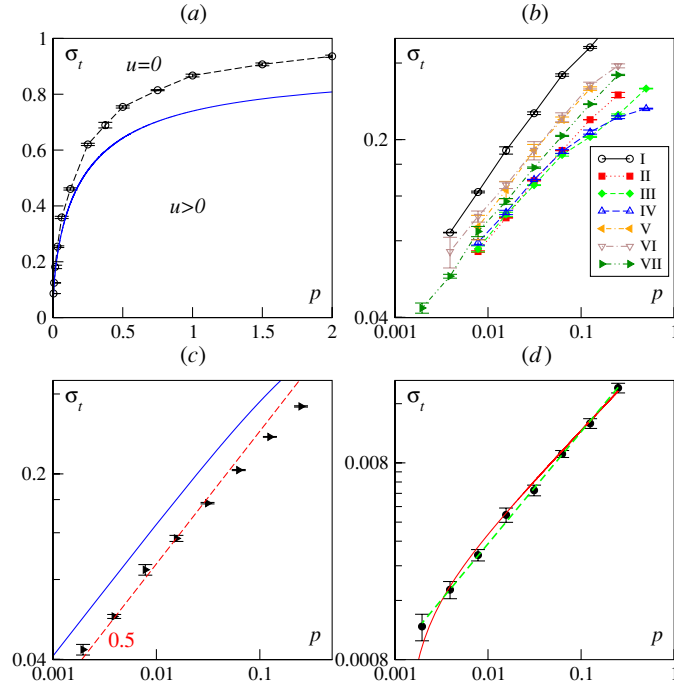


Figure 4. Phase diagram of agent-based models. (a) Overview of the phase diagram. The continuous line is the transition line of the continuous model given in equation (37); data for symbols \circ are obtained with the parameter set I. (b) Diagrams for all configurations with the self-diffusion noise $\sigma_0 = \sigma$ (plot in log–log scales). (c) Scaling of the transition line at small p with the set of parameters VII ($B = 64$) in log–log scales. The continuous line is the transition line (37) obtained from the kinetic theory. The dashed line is a square-root fit of the numerical results. (d) Model with a constant and maximum noise amplitude for self-diffusion in log–log scales (set VIII, $B = 64$). The continuous line corresponds to a fit of the numerical points with the law $\sigma_t = \alpha(p - p_t^0)^{1/2}$. The dashed line is a fit with a power law $\beta = 0.57$ (see table 1 for values of the other parameters).

4.3.3. Maximal self-diffusion. When we set the amplitude of self-diffusion noise to its maximum ($\eta_0 = 1$ or $\sigma_0 = \pi/\sqrt{3}$), the behaviour of the model remains qualitatively similar to the case $\sigma = \sigma_0$ that we studied above, with only a few quantitative differences. The transition line is shifted to a lower noise amplitude: σ_t differs by two orders of magnitude between the two comparable parameter sets VII and VIII. Fitting the two curves by a power law, the exponents are significantly different: $\beta \approx 0.46$ for set VII ($\sigma = \sigma_0$), while $\beta \approx 0.57$ for set VIII ($\sigma_0 = \sigma_0^{\max}$). One possible explanation for such a difference would be that, as in the hydrodynamic equations, there exists a threshold p_t^0 below which no collective motion occurs, whatever the noise amplitude σ . A fit with the function $p = \alpha\sqrt{p - p_t^0}$ gives a value $p_t^0 = 0.00133$ (figure 4(d)), much smaller than the theoretical value $p_t^0 = 3\pi/8 \approx 1.18$. Given the presently available data, we are not able to discriminate between the two fits and to conclude on the existence of a non-zero threshold value p_t^0 . Trying to find a phase transition for a very low value of p ($p = 2^{-10}$), below the fitted value p_t^0 , we could hardly define a threshold. However, it might be necessary to reach larger system sizes to detect a phase transition in this regime.

5. Beyond the strict validity domain of the hydrodynamic equations

In section 4, we concluded from a linear stability analysis that the homogeneous flow is unstable with respect to long wavelength perturbations, in the validity domain of the hydrodynamic equations, namely close to the transition line. When getting farther from the transition line, previous theoretical approaches [18] suggest that the homogeneous motion should be stable. To come to a conclusion in the present framework, it is thus necessary to come back to an analysis of the Boltzmann equation. It is also natural to wonder whether the hydrodynamic equations could yield, out of their strict validity domain, a qualitative description of the phenomenology of the moving phase. We address these issues in the present section. In particular, we find a restabilization of the homogeneous flow far from the transition line, as well as solitary waves that we compare with the travelling stripes already reported in numerical simulations of the agent-based model [14].

5.1. Stability analysis from the Boltzmann equation

In order to analyse the stability of the finite velocity solution beyond the validity domain of the hydrodynamic equations, we come back to the Boltzmann equation, and we resort to a semi-analytical treatment.

We start with a formal expansion of the phase-space distribution $f(\mathbf{r}, \theta, t)$ around the homogeneous stationary solution $f_0(\theta)$:

$$f(\mathbf{r}, \theta, t) = f_0(\theta) + \delta f(\mathbf{r}, \theta, t), \quad (58)$$

and we consider a perturbation of wave vector \mathbf{q} of the form

$$\delta f(\mathbf{r}, \theta, t) = \delta \rho_0 G(\theta, \mathbf{q}) e^{st + i\mathbf{q} \cdot \mathbf{r}}, \quad (59)$$

with $\int_{-\pi}^{\pi} d\theta G(\theta, \mathbf{q}) = 1$. Assuming, as in section 4.2.3, that both \mathbf{q} and the velocity perturbation are along the same direction \mathbf{e} as the collective velocity, the function $G(\theta, \mathbf{q})$ satisfies the following linearized Boltzmann equation:

$$sG(\theta, \mathbf{q}) + iqv_0 \cos \theta G(\theta, \mathbf{q}) = I_{\text{dif}}[G] + I_{\text{col}}[G, f_0] + I_{\text{col}}[f_0, G]. \quad (60)$$

Setting $\mathbf{q} = q\mathbf{e}$, we are interested in a small q expansion of equation (60), in order to compare with the results of equation (55). We then expand s and $G(\theta, \mathbf{q})$ in the following way:

$$s = is_1 q + s_2 q^2 + \mathcal{O}(q^3), \quad (61)$$

$$G(\theta, \mathbf{q}) = G_0(\theta) + iqG_1(\theta) + q^2 G_2(\theta) + \mathcal{O}(q^3), \quad (62)$$

with the normalization conditions:

$$\int_{-\pi}^{\pi} d\theta G_0(\theta) = 1, \quad \int_{-\pi}^{\pi} d\theta G_1(\theta) = 0, \quad \int_{-\pi}^{\pi} d\theta G_2(\theta) = 0. \quad (63)$$

Then G_0 , G_1 and G_2 are solutions of the hierarchy of equations

$$I_{\text{dif}}[G_0] + I_{\text{col}}[G_0, f_0] + I_{\text{col}}[f_0, G_0] = 0, \quad (64)$$

$$s_1 G_0(\theta) + v_0 \cos \theta G_0(\theta) = I_{\text{dif}}[G_1] + I_{\text{col}}[G_1, f_0] + I_{\text{col}}[f_0, G_1], \quad (65)$$

$$-s_1 G_1(\theta) + s_2 G_0(\theta) - v_0 \cos \theta G_1(\theta) = I_{\text{dif}}[G_2] + I_{\text{col}}[G_2, f_0] + I_{\text{col}}[f_0, G_2]. \quad (66)$$

Using the properties of I_{dif} and I_{col} , namely

$$\int_{-\pi}^{\pi} d\theta I_{\text{dif}}[g] = 0, \quad \int_{-\pi}^{\pi} d\theta I_{\text{col}}[g, f_0] = \int_{-\pi}^{\pi} d\theta I_{\text{col}}[f_0, g] = 0 \quad (67)$$

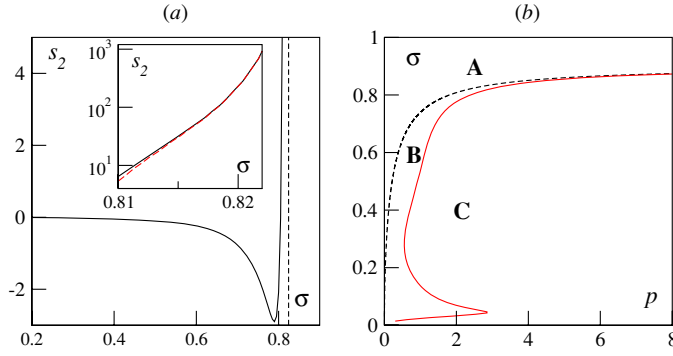


Figure 5. (a) Dependence of s_2 on σ for $p = 2.5$ and $\sigma_0 = \sigma$. For σ below a given threshold σ_t , s_2 becomes negative, indicating that the homogeneous state of motion is stable with respect to long wavelength perturbations. In contrast, close to the transition line, this state is unstable since $s_2 > 0$. The vertical dashed line corresponds to the transition value σ_t . Inset: comparison, close to σ_t , of s_2 obtained numerically from the Boltzmann equation (full line) and analytically from the hydrodynamic equations (dashed line), showing a good agreement. (b) Phase diagram indicating, for $\sigma = \sigma_0$, the three different regions: no motion (A), unstable homogeneous motion (B), stable homogeneous motion (C). The full line has been obtained numerically from a stability analysis of the Boltzmann equation. The dashed one is the transition line shown in figure 1(a).

for any function g , we obtain

$$s_1 = -v_0 \int_{-\pi}^{\pi} d\theta \cos \theta G_0(\theta), \quad (68)$$

$$s_2 = v_0 \int_{-\pi}^{\pi} d\theta \cos \theta G_1(\theta). \quad (69)$$

Hence the determination of G_2 is not necessary to compute s_2 . We only need to compute the hierarchy of functions up to G_1 . It is actually convenient to work in Fourier space, introducing the Fourier series expansion $\hat{G}_{0,k}$ and $\hat{G}_{1,k}$ of $G_0(\theta)$ and $G_1(\theta)$, respectively. In terms of this Fourier expansion, one finds $s_1 = -\hat{G}_{0,k=1}$ and $s_2 = \hat{G}_{1,k=1}$, assuming that $G_0(\theta)$ and $G_1(\theta)$ are even functions.

The integral equations (64) and (65) can be solved numerically, once expressed in terms of Fourier coefficients. To this purpose, we use the following Fourier expansion of the integral operators I_{dif} and I_{col} :

$$\int_{-\pi}^{\pi} d\theta e^{ik\theta} I_{\text{dif}}[g] = -\lambda(1 - e^{-k^2 \sigma_0^2/2}) \hat{g}_k, \quad (70)$$

$$\int_{-\pi}^{\pi} d\theta e^{ik\theta} I_{\text{col}}[g, h] = \frac{2d_0 v_0}{\pi} \sum_{q=-\infty}^{\infty} (e^{-k^2 \sigma^2/2} I_{q-\frac{k}{2}} - I_q) \hat{g}_{k-q} \hat{h}_q. \quad (71)$$

Numerical results are reported in figure 5(a), where s_2 is shown as a function of σ for $\sigma = \sigma_0$, all other parameters being kept fixed. Consistently with the results obtained from the hydrodynamic equations, we observe that close to the transition line, s_2 is positive and diverging. But for smaller values of the noise amplitude σ , s_2 becomes negative. Hence the homogeneous state of motion becomes stable in this range with respect to long wavelength perturbations.

As summarized in figure 5(b), there are from the point of view of stability three regions in the phase diagram (we focus here on the case $\sigma = \sigma_0$). These three regions can be described as follows:

- A** At low p or high σ , no collective motion occurs.
- B** For $p_t < p < p_r$, a homogeneous stationary solution with nonzero velocity exists, but it is unstable under longitudinal compression modes.
- C** For $p > p_r$, the homogeneous and stationary moving phase is linearly stable under any small perturbation.

p_r is defined as the value of the reduced density such that $s_2 = 0$. Note that p_r is not a monotonous function of σ . In the **B** region, the system cannot converge to a homogeneous stationary solution, and one thus expects the system to organize into more complicated spatio-temporal structures, that we shall try to describe in section 5.3.

5.2. Restabilization of the homogeneous flow in the hydrodynamic equations

The above stability analysis from the Boltzmann equation shows that the homogeneous flow becomes linearly stable when getting farther from the transition line p_t . Although this region of restabilization is, strictly speaking, out of the validity domain of the hydrodynamic equations, it would be interesting to know whether these equations already contain, at a qualitative level of description, the restabilization phenomenon.

One possible way to investigate this stability issue is to study the sign of the coefficient s_2 of the q^2 term in the small q expansion of $\Re[s_+]$. An equivalent procedure, that we follow here, is to look for the domain of existence of the wavenumber q_i (defined as $\Re[s_+] = 0$ for $q_i \neq 0$), when the control parameter p is increased at a given noise amplitude σ . In order to achieve this task, we solve the equation $\Re[s_+] = 0$, using expression (54). The solutions are naturally expressed in terms of the variable q_i^2 . After some algebra, we find for the largest solution

$$q_i^2 = \frac{\mu}{\nu v_0^2} \left[-\gamma w_1^2 \left(\frac{\mu'}{\mu} - \frac{\xi'}{\xi} \right) - 2v_0^2 + w_1 \left(\frac{\mu'}{\mu} - \frac{\xi'}{\xi} \right) \sqrt{\gamma^2 w_1^2 + 2v_0^2} \right], \quad (72)$$

where the term $\left(\frac{\mu'}{\mu} - \frac{\xi'}{\xi} \right)$ is positive. The expression on the right-hand side of equation (72) is positive for p close enough to p_t , and becomes negative for larger p (see figure 6(a)), in which case a real solution q_i does not exist. As a result, there exists a value p_r of the control parameter p such that q_i is no longer defined. For $p > p_r$, $\Re[s_+]$ remains negative for all values of q (figure 3(a)), so that all perturbations are linearly stable. Using equations (28)–(32), we can compute the restabilization line $p_r(\sigma)$ and show that p_r depends only on σ and σ_0 , but not on B . We also find that $p_r(\sigma)$ behaves for small noise amplitude as $p_r \propto \sigma^{1/2}$ (see figure 6(b) and its inset).

Altogether, the hydrodynamic equations seem to lead to the correct phenomenology even when used beyond their strict validity domain. Yet, the locations of the transition line $p_r(\sigma)$ predicted from the hydrodynamic equations on one side, and the one predicted from a long wavelength perturbative treatment of the Boltzmann equation on the other side, are quantitatively different, as illustrated in figures 5(b) and 6(b).

5.3. Inhomogeneous travelling solutions and solitary waves

For p slightly larger than p_t , the homogeneous solutions $\mathbf{w} = 0$ and $\mathbf{w} = \mathbf{w}_1$ are unstable, and one should look for the onset of spatio-temporal structures rather than purely stationary states. In this respect, one may be guided by the observations made in numerical simulations

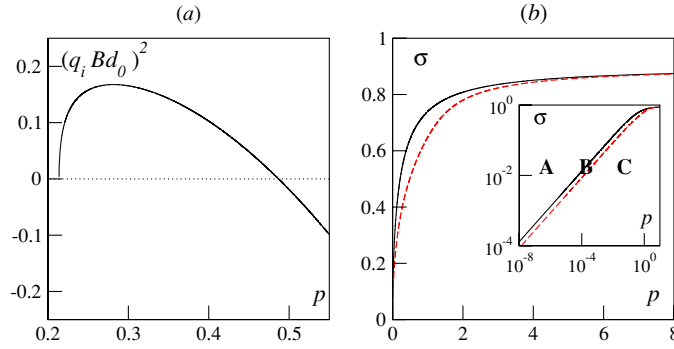


Figure 6. Restabilization in the hydrodynamic framework. (a) $(q_i B d_0)^2$ such that $\Re[s] = 0$ versus p , same parameters as figure 3. (b) Phase diagram. The full line corresponds to the onset of motion, σ_i . The dashed line is the transition between stable and unstable homogeneous flows, σ_r . Inset: same as (b) in the log-log scale. Regions **A**: $w = 0$, **B**: $w \neq 0$ and $\Re[s] > 0$ when $q < q_i$, **C**: $w \neq 0$ and $\Re[s] < 0$ for all q and for all direction of perturbation.

[14, 15], where ‘stripes’ of higher density moving over a low density background have been reported. Such structures are rather similar to soliton solutions that have been observed in many different physical contexts [21].

5.3.1. Stationary hydrodynamic equation in a moving frame. Let us now look for possible soliton solutions of the hydrodynamic equations (11) and (27). To this aim, we assume for ρ and \mathbf{w} the following ‘propagative’ form, with propagation velocity $c > 0$, along an arbitrary axis x of unit vector \mathbf{e} :

$$\rho(\mathbf{r}, t) = R(x - ct), \quad \mathbf{w}(\mathbf{r}, t) = W(x - ct) \mathbf{e}, \quad (73)$$

with $\zeta = x - ct$ and $W(\zeta) > 0$. Using equations (11), one finds the simple relation $R' = W'/c$, leading to

$$R(\zeta) = \frac{1}{c} W(\zeta) + \rho^*, \quad (74)$$

where ρ^* is up to now an arbitrary constant density. In the following, we consider velocity profiles that vanish for $\zeta \rightarrow \pm\infty$, so that $\rho^* = \lim_{\zeta \rightarrow \pm\infty} R(\zeta)$. Inserting this form in equation (27), one can eliminate $R(\zeta)$ and obtain the following ordinary differential equation for $W(\zeta)$, also taking into account the density dependence of the transport coefficients⁵:

$$W'' = -(a_0 - a_1 W - a_2 W')W' - b_1 W - b_2 W^2 - b_3 W^3. \quad (75)$$

The different coefficients in equation (75) read

$$a_0 = \left(c - \frac{v_0^2}{2c}\right) (D_1 + D_2 \rho^*) \quad (76)$$

$$a_1 = \tilde{\gamma} + D_2 \left(\frac{v_0^2}{2c^2} - 1\right) \quad (77)$$

$$a_2 = \frac{D_2}{c(D_1 + D_2 \rho^*)} \quad (78)$$

⁵ We however neglect the density dependence of the ratio v'/v , as it would lead to terms of higher order than those retained in our hydrodynamic description.

$$b_1 = \mu'(\rho^* - \rho_t)(D_1 + D_2\rho^*) \quad (79)$$

$$b_2 = \frac{\mu'}{c}[D_1 + D_2(2\rho^* - \rho_t)] \quad (80)$$

$$b_3 = \frac{\mu'D_2}{c^2} - \tilde{\xi} \quad (81)$$

with

$$D_1 = \frac{4\lambda}{v_0^2}(1 - e^{-2\sigma_0^2}) \quad (82)$$

$$D_2 = \frac{64d_0}{3\pi v_0} \left(\frac{7}{5} + e^{-2\sigma^2} \right), \quad (83)$$

and $\tilde{\gamma} = \gamma/v$, $\tilde{\xi} = \xi/v$. As often in the study of solitons [21], equation (75) may be reinterpreted as the equation of motion of a fictive particle with position W at time ζ . Here, this virtual particle has a unit mass, and moves in a potential

$$\Phi(W) = \frac{b_1}{2}W^2 + \frac{b_2}{3}W^3 + \frac{b_3}{4}W^4, \quad (84)$$

with a nonlinear friction force $-(a_0 - a_1W - a_2W')W'$. Depending on the sign of the effective friction coefficient $(a_0 - a_1W - a_2W')$, the friction force may either dissipate or supply energy to the particle. Note that this friction term breaks the symmetry $\zeta \rightarrow -\zeta$, so that the resulting momentum profile cannot be symmetric.

5.3.2. Numerical integration of the velocity and density profiles. To find a solution for $W(\zeta)$, we integrate numerically equation (75) for given values of the parameters a_i and b_i . The following constraints are imposed to the solution: $W(\zeta)$ should be positive for all values of ζ and $W(\zeta)$ should go to 0 for $\zeta \rightarrow \pm\infty$. Hence for large values of $|\zeta|$, $W(\zeta)$ should be small and should satisfy, to a good accuracy, the linearized version of equation (75), namely

$$W'' + a_0W' + b_1W = 0. \quad (85)$$

This equation has two exponential solutions $W_{\pm}(\zeta) = A_{\pm} \exp(r_{\pm}\zeta)$, with

$$r_{\pm} = \frac{1}{2} \left(-a_0 \pm \sqrt{a_0^2 - 4b_1} \right). \quad (86)$$

For $W(\zeta)$ to be positive, one needs that the roots r_{\pm} be real, which implies $a_0^2 - 4b_1 \geq 0$. Further, for $W(\zeta)$ to vanish both for $\zeta \rightarrow -\infty$ and $\zeta \rightarrow +\infty$, one should have both an increasing and a decreasing solution for equation (85), namely $r_+ > 0$ and $r_- < 0$, which corresponds to $b_1 < 0$.

The free parameters in equation (75) are c and ρ^* (this point will be briefly discussed in section 5.4, in connection with numerical results). The noises σ and σ_0 are external control parameters. The overall density ρ is computed afterwards from the profile $R(\zeta)$. Assuming that we are in the low noise region of parameter space $\sigma < \sigma_t^\infty$, then $[\exp(-\sigma^2/2) - 2/3] > 0$ and the condition $b_1 < 0$ implies $\rho^* < \rho_t$. In addition, as the trajectory of the particle starts and ends at the same position $W = 0$ with zero velocity ($W' = 0$), its energy is the same, which means that the friction force has to dissipate energy on some part of the trajectory and to supply energy otherwise. Assuming $a_0 > 0$ implies $c - v_0^2/(2c) > 0$, that is $c > v_0/\sqrt{2}$. On the other hand, one intuitively expects c to be smaller than the microscopic velocity v_0 of the particles.

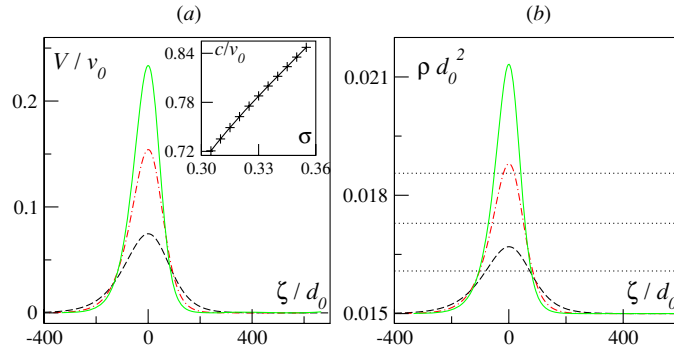


Figure 7. (a) Velocity profile $v(x, t) = V(\zeta)$, with $\zeta = x - ct$, for $\rho^* = 0.06$ and $\sigma = \sigma_0 = 0.31$ (dashed line), 0.32 (dot-dashed line) and 0.33 (full line). Inset: propagation velocity c as a function of σ . (b) Density profile $\rho(x, t) = R(\zeta)$ for the same values of the parameters. Horizontal dotted lines correspond to the density ρ_t for $\sigma = \sigma_0 = 0.31, 0.32$ and 0.33 (bottom to top). Other parameters: $\lambda = 0.5, d_0 = 0.5$ and $v_0 = 1$.

The numerical procedure we implement is the following. Choosing a given value for ρ^* and for c , we start at $\zeta = \zeta_0 < 0$ ($|\zeta_0| \gg 1$), with a small value $W(\zeta_0) = W_0 \ll 1$, and with a derivative $W'(\zeta_0) = r_+ W_0$. This choice of initial conditions ensures that we select a solution with an exponential tail $W(\zeta) = A_+ \exp(r_+ \zeta)$ for $\zeta < \zeta_0$. Then we integrate numerically the differential equation for $\zeta > \zeta_0$, until reaching large enough positive values of ζ . At this stage, two behaviours may appear. One should first notice that for $b_1 < 0$ (and at least if b_3 does not take a large negative value) the effective potential $\Phi(W)$ has a local maximum in $W = 0$ and a local minimum at a value $W = W_{\min}$. Then, if the dissipated energy is larger than the injected energy, the particle ends up at W_{\min} for $\zeta \rightarrow \infty$, yielding a profile $W(\zeta)$ that does not fulfil the condition required. In the opposite case, if energy injection dominates, the particle crosses the local maximum at $W = 0$ and goes to negative values. It is only in the marginal case where dissipation exactly compensates injection that the correct profile $W(\zeta)$ is found. As friction is mainly controlled by the parameter c , we keep ρ^* fixed and perform a loop over the value of c in order to converge towards the marginal solution. Note, however, that if $b_3 < 0$, $\Phi(W) \rightarrow -\infty$ when $W \rightarrow +\infty$, so that one should also take care that the particle does not ‘escape’ to large positive values of W .

Using the above procedure, we obtain a family of profiles $W(\zeta)$ with three control parameters, namely the ‘background’ density ρ^* and the noises σ and σ_0 . In the following, we restrict ourselves to the case $\sigma_0 = \sigma$. The density profile is computed from the relation $R(\zeta) = \rho^* + W(\zeta)/c$, and the velocity profile $V(\zeta)$ is obtained from the momentum profile $W(\zeta)$ through $V(\zeta) = W(\zeta)/R(\zeta)$. Examples of such velocity profiles are presented in figure 7, for different values of σ and for a given value of ρ^* .

A remaining open issue is the stability of these solitary waves with respect to small perturbations. A formal stability analysis like the one performed for the homogeneous state of motion is a difficult task here, and we leave this question for future work.

5.4. Solitary waves in the agent-based model

We now compare the solitary waves computed in the hydrodynamic equations with the travelling stripes observed in direct numerical simulations of the agent-based model (see figure 8(a)). We focus again on the case $\sigma_0 = \sigma$. The stripped structures are composed

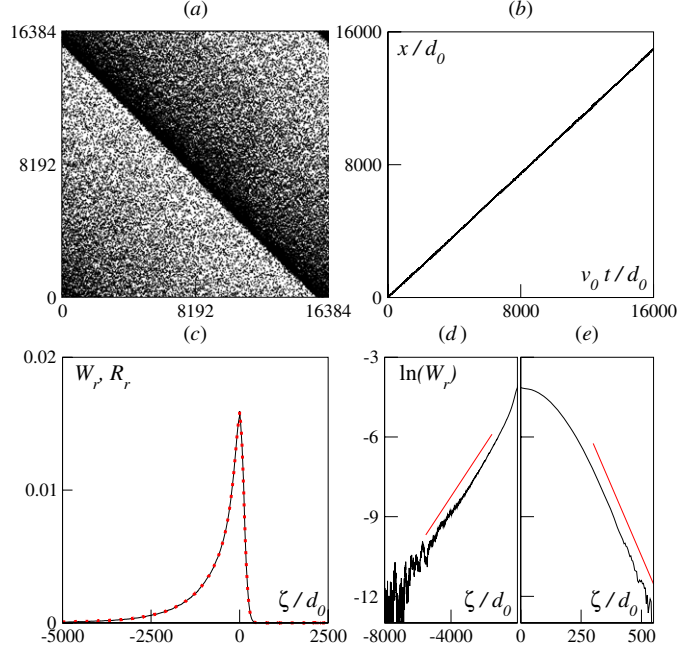


Figure 8. Solitons in the numerical model. (a) Instantaneous snapshot, the band is moving southwest; lengths are scaled by d_0 . (b) Example of trajectory in the direction of the averaged velocity. (c) Mean profiles along the direction of the main motion. We plot the reduced dimensionless density $R_r = (\langle \rho(x - ct) \rangle - \rho^{\text{sat}}) d_0^2 c / v_0$ (dotted line) and the dimensionless momentum $W_r = \langle w(x - ct) \rangle d_0^2 / v_0$ (plain line), both being time-averaged in the comoving frame of the soliton. (d and e) Same data as (c) on semi-log scales, emphasizing the exponential decay. The scales are identical on vertical axes, but different on abscissas. Parameter values are $p = 2^{-3}$, $\sigma = 0.163$, $L = 4096$; the other ones correspond to set VII in table 1.

of several localized, randomly spaced bands. They are not part of a regular pattern, nor a wave train [15]. They are all moving along the direction of the main motion, although during the transient period they can pass through each other with only few interactions. The space between two bands is filled with particles moving independently (the hydrodynamic momentum vanishes) and homogeneously (the density is constant). In analogy to the liquid–gas coexistence, we denote this state as the *saturating vapour*.

We observe that the bands move at a constant speed, at least on the duration necessary to travel through the system size (figure 8(b)). From the trajectories, we measured the velocity c of the solitons. On the density profiles, we extracted the value ρ^{sat} of the density outside the peak. If these structures are only propagative and if the continuity equation is valid at a coarse-grained level in the agent-based model (which is expected from mass conservation), the density and momentum profiles should be related by $W = c(R - \rho^{\text{sat}})$, as in section 5.3. Plotting on figure 8(c) both the reduced density $c(R - \rho^{\text{sat}})$ and the momentum W , we observe that both curves match perfectly, confirming the propagative nature of this striped pattern.

These solitary waves are quite similar to the soliton we found in the hydrodynamic equations (see section 5.3), with an exponential decay of the momentum profile on both sides (figure 8(d–e)) in particular. However, the asymmetry of the profile is much more pronounced

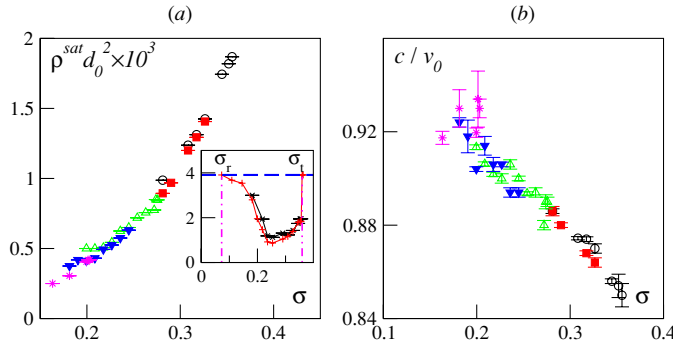


Figure 9. Solitons in the numerical model. (a) Density of saturated vapour for different p ($p = 2^{-2}$, \circ ; 5^{-1} , \blacksquare ; 2^{-3} , \triangle ; 10^{-1} , \blacktriangledown and 2^{-4} , $*$). Inset: finite size effects on soliton, $p = 2^{-4}$, $L = 1024$ (\times) and $L = 2048$ ($+$). The dashed line marks the value of the global density ($\rho = 2^{-5}$). The dotted lines underline the threshold of the collective motion σ_t and of the homogeneous moving population σ_r . (b) Speed of the solitons (same parameters). The other parameters are the ones of set VII (see table 1).

than in the analytical model: the exponential decay is much steeper in front of the profile than in the rear part.

We now study how the two main characteristics of the solitary waves, namely the velocity c and the density ρ^{sat} , vary with the control parameters p and σ . Since we perform a numerical study, we need to be aware of finite size effects. Plotting the density of saturating vapour versus noise for a given density but for different sizes, we can make three observations (inset of figure 9). First, the system size hardly changes ρ^{sat} provided that the noise amplitude remains near the threshold. Moreover, at a lower noise amplitude, the density ρ^{sat} increases and become sensitive to the system size. Lastly, there is a noise σ_r below which we cannot observe solitons anymore (see also [15]) and the system becomes homogeneous at a coarse-grained level. The result is qualitatively consistent with the restabilization of the homogeneous flow described in sections 5.1 and 5.2.

The study of the very low noise amplitude region of the phase diagram is an ongoing work. So we mainly focused in the present paper on the region relatively close to the transition to collective motion. For different global densities, both ρ^{sat} and c fall onto the same curve when plotted as a function of σ , as shown on figure 9(a) and (b). Therefore, once the noise amplitude σ is given, the characteristics (c , ρ^{sat}) of the solitary waves are determined, and the number of solitary waves is adjusted by the dynamics in order to match the global density of the system.

This is a major difference with the solitary waves obtained from the hydrodynamic equations in section 5.3. These solitary waves depend on two control parameters, namely the noise amplitude σ and the density at infinity ρ^* . Hence there is *a priori* no way to determine the number of solitons in a large but finite system with a given density. At a heuristic level, we might guess that the solitary waves may be stable only for some specific values of ρ^* , which would give a selection mechanism for the density ρ^{sat} . Such a mechanism would make the connection between the analytical and numerical models clearer, but we presently have no clue to confirm this tentative scenario. Obviously, further studies of the dynamics of the solitary waves in the context of the hydrodynamic equations are needed.

6. Conclusion

In summary, we have derived in this paper hydrodynamic equations for a model of self-propelled particles with binary interactions, in the regime of low hydrodynamic velocity. We also compared the results of the hydrodynamic description to the numerical simulations of a standard agent-based model. In the analytical model, the homogeneous state with zero velocity is a stationary solution for any values of the microscopic parameters (the noise amplitude and the overall density), but this state is linearly unstable for a reduced density p greater than a transition density $p_t(\sigma)$, or equivalently, for a noise smaller than a transition value $\sigma_t(p)$.

When the zero velocity solution is unstable, another homogeneous state, with a nonzero hydrodynamic velocity, appears. This state is linearly stable with respect to spatially homogeneous perturbations. However, close to the transition line $\sigma_t(p)$, this state turns out to be linearly unstable with respect to finite wavelength perturbations. As the validity of the hydrodynamic equations is, strictly speaking, restricted to the vicinity of the transition line, we also studied the stability of the homogeneous state of motion directly from the Boltzmann equation. We found that, far enough from the transition line, the homogeneous motion becomes linearly stable. Interestingly, this restabilization phenomenon is also qualitatively observed in the hydrodynamic equations, although this regime is beyond their domain of validity. All these results agree semi-quantitatively with the numerical simulations of the agent-based model.

When the homogeneous state of motion is unstable, more complex spatio-temporal structures should appear. A candidate for such structure is the solitary waves we obtained from the hydrodynamic equations. These solitary waves resemble the moving stripes observed in the numerical agent-based model, apart from the asymmetry which is more pronounced in the latter. A word of caution is however needed here, as on the one hand the solitary waves have a finite amplitude, so that the hydrodynamic equations might not be valid, and more importantly, their stability has not been tested yet. On the basis of the numerical simulations of the agent-based model, it is however likely that these solitary waves should be stable at least in a given region of the phase diagram.

As for future work, it would be interesting to investigate the stability of the solitary waves, and to look for possible ‘multi-soliton’ solutions, in case the stability would be confirmed. Specifically, it would be interesting to be able to determine the number of solitons, their celerity and the background density as a function of the global density (for a finite volume) and of the noise amplitude, if such a relation exists, as suggested by the numerical simulations of the agent-based model.

Acknowledgments

This research work has been partly supported by the French ANR project ‘DyCoAct’ and by the Swiss National Science Foundation. EB is grateful to R Presle for his contribution in an early stage of this work.

Appendix A. Agent-based model

A.1. Looking at the model further

The numerical system we looked at is very similar to the one defined by Vicsek *et al* [12]. This is a very minimal model, easy to implement. In contrast, a real direct simulation would have been coded following a molecular dynamics algorithm, which would have cost much more cpu time than our Monte Carlo-like program. The numerical choice is also related to the fact

that collective motion of self-propelled particles has been mainly studied in this framework during the last 10 years [13–15, 22–30]. Thus we would like to take profit from this large background and the knowledge of the system we already got.

To fully understand the results presented in this paper, we must explain the differences between the numerical system we used and a direct simulation. In what we have done, collisions are computed at a fixed time step. So every other collision that could have occurred within Δt is neglected. On the other hand, collisions can involve many individuals. Another implication of the discrete time step is that decreasing the time step increases the collision frequency. Then the noise does not act on the system with the same manner for two different time steps. Hence, in its present formulation, the agent-based model is not a discretized version of a continuous time model. To reach this goal, the noise amplitude should be renormalized in some way with the time step.

The balance of the above different effects is difficult to imagine *a priori*. We do not expect any *quantitative* matching between the theory we developed and the simulations we presented. But we still want to test the robustness of the predictions made for large system sizes.

We must also emphasize that some studies in the literature were aimed at giving an exact continuous theory of Vicsek's model [31–33]. Up to now, this difficult problem has been dealt in the framework of perturbative theories at a first order in speed differences. In addition, the role of the noise is not properly taken into account in these studies: it is either ignored [31] or described by a phenomenological diffusive term [32]. Finally, the transport coefficients of the hydrodynamic equation do not contain any dependence on the microscopic parameters of the model.

A.2. Phase transition

As in usual versions of self-propelled particle systems, the behaviour of the system roughly falls into two different categories. Either there is no collective motion: every particle moves randomly without clear correlation with its neighbours, or there is a non-zero global velocity in an arbitrary direction.

Since the analogy with magnetic systems is quite obvious, the habit is to consider the equivalent averaged magnetization of our system, namely the global normalized velocity φ^t :

$$\varphi^t = \left\| \frac{1}{N v_0} \sum_{j=1}^N \mathbf{v}_j^t \right\|, \quad (\text{A.1})$$

considered as an order parameter. To determine the characteristics of the phase transition, we study the statistical properties of the order parameter φ^t , considering its mean $\langle \varphi \rangle$, its variance χ and its Binder cumulant K [34]:

$$\langle \varphi \rangle = \frac{1}{T} \sum_{t=1}^T \varphi^t, \quad (\text{A.2})$$

$$\chi = L^2 (\langle \varphi^2 \rangle - \langle \varphi \rangle^2), \quad (\text{A.3})$$

$$K = 1 - \frac{\langle \varphi^4 \rangle}{3 \langle \varphi^2 \rangle^2}. \quad (\text{A.4})$$

The brackets $\langle \dots \rangle$ indicate an averaging over time. The duration of the simulation has to be large to inhibit memory effects. Ideally, the correlation time for each set of parameters

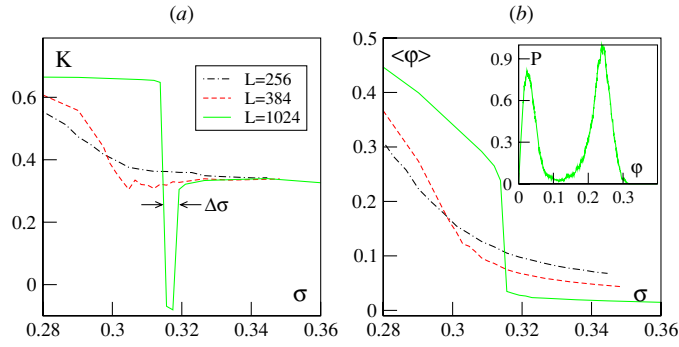


Figure A1. Phase transition in numerical simulation and finite size effects. We plotted (a) the Binder cumulant K and (b) the averaged order parameter $\langle\phi\rangle$ versus noise rms-value, for three different sizes. In the inset, we show the histogram of the order parameter ϕ at the transition point for a system size $L = 1024$. In (a), we emphasized the depth of the well $\Delta\sigma$: approximation of the errors in determining the transition point. Parameters are the ones of configuration III with $\rho = 1/16$ or $p = 1/2$.

$(\rho, \sigma, \sigma_0, v_0, d_0, \lambda)$ should be computed from the auto-correlation function [35]. However, this is a tantamount task⁶. Practically, in order to have a rough approximation of the correlation time, we measured the transition time from the initial condition to the stationary state. Then we performed averaging on time which are hundred times greater than that transition time.

For all sets of parameters I–VII (table 1), we observed that the system exhibits a phase transition from a non-moving to a globally moving population when decreasing the noise amplitude at a fixed density. At small enough size L , all statistical variables ($\langle\phi\rangle, \chi, K$) remain continuous, while a singular point appears when the system is larger than a typical size L_t (see figure A1(a) and (b), as well as [14, 15]).

The main observations are the following: the order parameter curve exhibits a jump (figure A1(b)), the variance is delta-peaked (not shown here), the Binder cumulant has a minimum (figure A1(a)) which goes to larger negative values when the system size is increased and the histogram of the order parameter is bimodal (see inset of figure A1(b)). All these sign plead in favour of a first-order phase transition.

It is now well known that a finite size system exhibits a rounded transition, at equilibrium [36, 37] or far from the equilibrium [38, 39]. The scaling laws are normally sufficient to detect the order of the transition. In our case, the finite size scaling laws correspond to a continuous transition below L_t [40, 41] and to a discontinuous transition above L_t [15].

To estimate the transition point, we measured the location where the Binder cumulant minimum becomes negative. We neglected the finite size effects at higher size. We determined the error bars on that location as the width of the well (see figure A1(a)).

Appendix B. Stability against arbitrary perturbations

In this appendix, we study within the framework of the hydrodynamic equations the stability of the stationary homogeneous flow. Starting from equations (41) and (42), we consider the

⁶ The cumulative consumed cpu time already reaches 50 years.

case where $\mathbf{w}_0 = \mathbf{w}_1 \neq \mathbf{0}$, solution of equation (33). The rotational symmetry is broken when the collective motion appears, and we take $\mathbf{e}_\parallel = \mathbf{w}_1/|\mathbf{w}_1|$ as a first vector of the geometrical basis. Then we define two angles ϑ_1 and ϑ_2 between \mathbf{e}_\parallel and the directions of $\delta\mathbf{w}_0$ and \mathbf{q} , respectively. We denote as \mathbf{e}_\perp the unit vector orthogonal to \mathbf{e}_\parallel such that $(\mathbf{e}_\parallel, \mathbf{e}_\perp)$ form a direct basis.

From equations (44) and (45), we project the resulting vectorial equation onto \mathbf{e}_\parallel and \mathbf{e}_\perp , and we eliminate the ratio $\delta\mathbf{w}_0/\delta\rho_0$ from the continuity equation, yielding

$$s[s + i\gamma w_1 q \cos \vartheta_2 + \nu q^2] \cos \vartheta_1 = \left[-\frac{1}{2} v_0^2 q \cos(\vartheta_1 - \vartheta_2) + i s \kappa w_1 \cos \vartheta_1 \right] q \cos \vartheta_2 - [2s\xi w_1^2 \cos \vartheta_1 + i(\mu' - \xi' w_1^2 + s\kappa) q w_1 \cos(\vartheta_1 - \vartheta_2)], \quad (\text{B.1})$$

$$s[s + i\gamma w_1 q \cos \vartheta_2 + \nu q^2] \sin \vartheta_1 = \left[-\frac{1}{2} v_0^2 q \cos(\vartheta_1 - \vartheta_2) + i s \kappa w_1 \cos \vartheta_1 \right] q \sin \vartheta_2, \quad (\text{B.2})$$

where q and w_1 are real and positive. These are two polynomial equations that we will study at a given point (ρ, σ) of the phase diagram, for a set of physical variables (d_0, λ, v_0) and for different pairs $(\vartheta_1, \vartheta_2)$. For all fixed parameters, the solutions of those equations will be a discrete number of sets (q, s) .

First, one can check that this set of equations is invariant when $\delta\mathbf{w}_0$ is rotated with an angle of π ($\vartheta_1 \rightarrow \vartheta_1 + \pi$). Note also that every real term depends on an even power of q . So one can expect that the real part of the growth rate $\Re[s]$ only depends on even powers of q , and that $\Re[s]$ remains invariant when ϑ_2 is changed into $\vartheta_2 + \pi$. That is why we will study equations (B.1) and (B.2) for $(\vartheta_1, \vartheta_2) \in [0, \pi[\times [0, \pi[$.

A third property arises clearly when we introduce the expressions (28)–(32) of the transport coefficients in equations (B.1) and (B.2): the wavenumber q appears only through the product $q B d_0$, meaning that the solutions q are proportional to $1/B d_0$. As already mentioned, the framework of the kinetic approach implies that B is large, and therefore it implies that we are studying long wavelength perturbations. This analysis also shows that the growth rate depends only on the dimensionless control parameter p , the noise amplitudes σ and σ_0 , and the self-diffusion rate λ which gives the proper unit to s . Let us also mention that a trivial solution of the system of equations is $s = 0$ for $q = 0$. This solution is actually an artefact of the calculation procedure (namely a multiplication by s), as it is not a solution of the original equations (41) and (42). Hence we will not consider this extra solution in the following.

For some parameters $(\vartheta_1, \vartheta_2)$, one or several terms can vanish, and the degree of the polynomials may decrease. We will first study the general equations and those particular cases will be considered later. If we combine $((\text{B.1}) \times \sin \vartheta_1 - (\text{B.2}) \times \cos \vartheta_1)$, we get a linear equation in s :

$$s = -\frac{q \cos(\vartheta_1 - \vartheta_2)}{2w_1} \frac{q v_0^2 \sin(\vartheta_1 - \vartheta_2) + 2i w_1 (\mu' - \xi' w_1^2) \sin \vartheta_1}{2\xi w_1 \cos \vartheta_1 \sin \vartheta_1 + i q \kappa \sin \vartheta_2}. \quad (\text{B.3})$$

Indeed, we verify that $\Re[s]$ is an even function of q . Now we can replace s by its expression in equation (B.2). The resulting equation is a third-degree polynomial that can be formally written as

$$d_3 q^3 + i d_2 q^2 + d_1 q + i d_0 = 0, \quad (\text{B.4})$$

where the coefficients d_i are real functions of (p, σ, σ_0, B) and of $(\vartheta_1, \vartheta_2)$. The last three coefficients are rather difficult to manipulate. But this equation can be easily solved using Cardano's method for instance. In the case where

$$d_3 = \sin \vartheta_1 \sin \vartheta_2 \sin(\vartheta_1 - \vartheta_2) \cos(\vartheta_1 - \vartheta_2) \quad (\text{B.5})$$

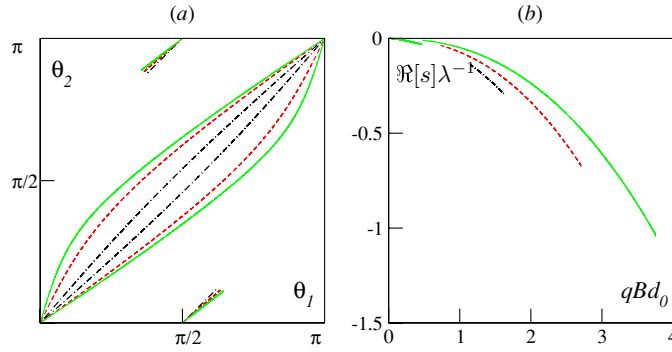


Figure B1. Stability against inhomogeneous perturbations, solutions of equations (B.3) and (B.4) so that $\Im[q] = 0$. (a) $(\vartheta_1, \vartheta_2)$, with $\sigma = \sigma_0 = 0.5$, $p = 0.22$ (dot-dashed line), 0.30 (dashed), 0.40 (full line). (b) $\Re[s]$ versus q , same parameters as (a), $\Re[s]$ increases when p increases.

does not vanish, we compute the solutions. The resulting values q are complex numbers, so that they cannot correspond to physical solutions. Yet, for some sets of angles $(\vartheta_1, \vartheta_2)$, the solutions for q are real. We are interested only in these modes. Determining the angles $(\vartheta_1, \vartheta_2)$ for which q is real, we then compute the growth rate $\Re[s_+]$ using equation (B.3). There are four different branches (see figures B1(a)), whose lengths increase when the control parameter is chosen deeper in the collectively moving phase (i.e. at low σ or at high p). For all sets of parameters for which we have computed the growth rate, its real part remains negative (figure B1(b)). Thus the homogeneous moving phase is stable against finite wavelength perturbations in the general case.

The above calculation relies on the assumption that $d_3 \neq 0$. This assumption is not valid in either of the following four cases:

- a longitudinal instability ($\sin \vartheta_1 = 0$),
- a wave vector \mathbf{q} colinear to the direction of the main motion ($\sin \vartheta_2 = 0$),
- a perturbation $\delta \mathbf{w}_0$ colinear to the wave vector \mathbf{q} ($\sin(\vartheta_1 - \vartheta_2) = 0$).
- a perturbation $\delta \mathbf{w}_0$ perpendicular to the wave vector \mathbf{q} ($\cos(\vartheta_1 - \vartheta_2) = 0$).

We first consider the study of stability under a longitudinal perturbation: \mathbf{w}_1 and $\delta \mathbf{w}_0$ are colinear. Then equation (B.2) vanishes in two cases:

$$s = -\frac{iqv_0^2 \cos \vartheta_2}{2\kappa w_1}, \quad \text{or} \quad \sin \vartheta_2 = 0.$$

Replacing s by the first expression in equation (B.1), we can show that there is no authorized mode, in other words $\Im[q] \neq 0$. So, equation (B.2) vanishes only for $\vartheta_1 = \vartheta_2 = 0$. The corresponding stability analysis is presented in detail in section 4.2.3.

For any of the last three cases, we solve equations (B.2) and (B.2), and we find that either there is no authorized mode (q is complex) or $\Re[s_+] \leq 0$. Thus none of those cases is related to an unstable mode.

To sum up, this study of the stability of the homogeneous stationary moving phase shows that the longitudinal direction is the only mode which can be unstable. This result is consistent with the observations made in numerical simulations [14, 15].

References

- [1] Toner J, Tu Y and Ramaswamy S 2005 *Ann. Phys.* **318** 170
- [2] Parrish J K and Hamner W M (eds) 1997 *Animal Groups in Three Dimensions* (Cambridge: Cambridge University Press)
- [3] Helbing D, Farkas I and Vicsek T 2000 *Nature* **407** 487
- [4] Helbing D, Farkas I J and Vicsek T 2000 *Phys. Rev. Lett.* **84** 1240
- [5] Feare C 1984 *The Starlings* (Oxford: Oxford University Press)
- [6] Hubbard S, Babak P, Sigurdsson S and Magnusson K 2004 *Ecol. Model.* **174** 359
- [7] Rauch E, Millonas M and Chialvo D 1995 *Phys. Lett. A* **207** 185
- [8] Ben-Jacob E, Cohen I, Shochet O, Czirók A and Vicsek T 1995 *Phys. Rev. Lett.* **75** 2899
- [9] Harada Y, Nogushi A, Kishino A and Yanagida T 1987 *Nature (Lond.)* **326** 805
- [10] Badoual M, Jülicher F and Prost J 2002 *Proc. Natl Acad. Sci. USA* **99** 6696
- [11] Sugawara K, Sano M and Watanabe T 2002 *Proc. of 2002 FIRA Robot World Congress* p 36
- [12] Vicsek T, Czirók A, Ben-Jacob E, Cohen I and Shochet O 1995 *Phys. Rev. Lett.* **75** 1226
- [13] Czirók A, Stanley H E and Vicsek T 1997 *J. Phys. A: Math. Gen.* **30** 1375
- [14] Grégoire G and Chaté H 2004 *Phys. Rev. Lett.* **92** 025702
- [15] Chaté H, Ginelli F, Grégoire G and Raynaud F 2008 *Phys. Rev. E* **77** 046113
- [16] Csahók Z and Czirók A 2002 *Physica A* **243** 304
- [17] Toner J and Tu Y 1995 *Phys. Rev. Lett.* **75** 4326
- [18] Toner J and Tu Y 1998 *Phys. Rev. E* **58** 4828–58
- [19] Bertin E, Droz M and Grégoire G 2006 *Phys. Rev. E* **74** 022101
- [20] Baskaran A and Marchetti M 2008 *Phys. Rev. Lett.* **101** 268101
- [21] Dauxois T and Peyrard M 2006 *Physics of Solitons* (Cambridge: Cambridge University Press)
- [22] Albano E V 1996 *Phys. Rev. Lett.* **77** 2129
- [23] Aldana M, Dossetti V, Huepe C, Kenkre V M and Larralde H 2007 *Phys. Rev. Lett.* **98** 095702
- [24] Aldana M and Huepe C 2003 *J. Stat. Phys.* **112** 135
- [25] Couzin I D 2002 *J. Theor. Biol.* **218** 1
- [26] Duparcmeur Y L, Herrman H and Troadec J P 1995 *J. Phys. I (France)* **5** 1119
- [27] Grégoire G, Chaté H and Tu Y 2001 *Phys. Rev. E* **64** 011902
- [28] Levine H, Rappel W J and Cohen I 2000 *Phys. Rev. E* **63** 017101
- [29] Mikhailov A S and Zanette D H 1999 *Phys. Rev. E* **60** 4571
- [30] Shimoyama N, Sugawara K, Mizuguchi T, Hayakawa Y and Sano M 1996 *Phys. Rev. Lett.* **76** 3870
- [31] Ratushnaya V I, Bedeaux D, Kulinskii V L and Zvelindovsky A V 2007 *Physica A* **381** 39–46
- [32] Degond P and Motsch S 2007 *Comptes-rendus Mathématiques* **345** 555–60
- [33] Degond P and Motsch S 2008 *J. Stat. Phys.* **131** 989–1021
- [34] Binder K 1976 *Phase Transitions and Critical Phenomena* ed C Domb and M S Green (New York: Academic)
- [35] Müller-Krumbhaar H and Binder K 1973 *J. Stat. Phys.* **8** 1
- [36] Privman V (ed) 1990 *Finite Size Scaling and Numerical Simulations of Statistical Systems* (Singapore: World Scientific)
- [37] Borgs C and Kotecký R 1990 *J. Stat. Phys.* **61** 79
- [38] Lübeck S 2004 *Int. J. Mod. Phys. B* **18** 3977–4118
- [39] Marcq P, Chaté H and Manneville P 2006 *Prog. Theor. Phys. Suppl.* **161** 244
- [40] Grégoire G 2002 *Mouvement Collectif et Physique hors d'équilibre PhD thesis* Université Paris 7–Denis Diderot
- [41] Baglietto G and Albano E V 2008 *Phys. Rev. E* **78** 021125